AFRL-RY-WP-TR-2016-0179

3-D INDEX DISTRIBUTION FOR GENERALIZED OPTICAL MEASUREMENT

Mark Neifeld

University of Arizona

DECEMBER 2016
Final Report

STINFO COPY

AIR FORCE RESEARCH LABORATORY
SENSORS DIRECTORATE
WRIGHT-PATTERSON AIR FORCE BASE, OH 45433-7320
AIR FORCE MATERIEL COMMAND
UNITED STATES AIR FORCE

NOTICE AND SIGNATURE PAGE

*//Signature//

ROBERT M. ZUMRICK
Program Manager
EO Target Detection and Surveillance Branch
Sensors Directorate

//Signature//

ALAN H. RATCLIFF, Chief
EO Target Detection and Surveillance Branch
Multispectral Sensing and Detection Division
Sensors Directorate

*//Signature//

TRACY W. JOHNSTON, Chief
Capacity regarding report
Multispectral Sensing and Detection Division
Sensors Directorate

REPORT DOCUMENTATION PAGE

Form Approved
OMB No. 0704-0188

1. REPORT DATE *(DD-MM-YY)*	2. REPORT TYPE	3. DATES COVERED *(From - To)*
December 2016	Final	19 March 2014 – 31 May 2016

4. TITLE AND SUBTITLE
3-D INDEX DISTRIBUTION FOR GENERALIZED OPTICAL MEASUREMENT

5a. CONTRACT NUMBER
FA8650-14-1-7408

5b. GRANT NUMBER

5c. PROGRAM ELEMENT NUMBER
69199E

6. AUTHOR(S)
Mark Neifeld

5d. PROJECT NUMBER
DARPA

5e. TASK NUMBER
N/A

5f. WORK UNIT NUMBER
Y0ZW

7. PERFORMING ORGANIZATION NAME(S) AND ADDRESS(ES)

University of Arizona
Tucson, AZ 85721

8. PERFORMING ORGANIZATION REPORT NUMBER

9. SPONSORING/MONITORING AGENCY NAME(S) AND ADDRESS(ES)

Air Force Research Laboratory
Sensors Directorate
Wright-Patterson Air Force Base, OH 45433-7320
Air Force Materiel Command
United States Air Force

Defense Advanced Research Projects Agency (DARPA/MTO)
675 North Randolph Street
Arlington, VA 22203-2114

10. SPONSORING/MONITORING AGENCY ACRONYM(S)
AFRL/RYMT

11. SPONSORING/MONITORING AGENCY REPORT NUMBER(S)
AFRL-RY-WP-TR-2016-0179

12. DISTRIBUTION/AVAILABILITY STATEMENT
Approved for public release; distribution is unlimited.

13. SUPPLEMENTARY NOTES
This material is based on research sponsored by Air Force Research laboratory (AFRL) and the Defense Advanced Research Agency (DARPA) under agreement number FA8650-14-1-7408. The U.S. Government is authorized to reproduce and distribute reprints for Governmental purposes notwithstanding any copyright notation herein. The views and conclusions contained herein are those of the authors and should not be interpreted as necessarily representing the official policies of endorsements, either expressed or implied, of Air Force Research Laboratory (AFRL) and the Defense Advanced Research Agency (DARPA) or the U.S. Government. PAO case number 88ABW-2016-6309, Clearance Date7 December 2016.Report contains color.

14. ABSTRACT
Optical measurement is central to a wide range of military and commercial applications. Leveraging the ease with which optical sensing may now be followed by sophisticated digital computing a new computational imaging (CI) paradigm has emerged in which algorithmic degrees of freedom are co-designed with the more traditional physical optical degrees of freedom to yield entirely new types of cameras.

15. SUBJECT TERMS
3-D index, generalized optical measurement

16. SECURITY CLASSIFICATION OF:			17. LIMITATION OF ABSTRACT:	18. NUMBER OF PAGES	19a. NAME OF RESPONSIBLE PERSON (Monitor)
a. REPORT Unclassified	**b. ABSTRACT** Unclassified	**c. THIS PAGE** Unclassified	SAR	40	Robert Zumrick
					19b. TELEPHONE NUMBER *(Include Area Code)* N/A

Standard Form 298 (Rev. 8-98)
Prescribed by ANSI Std. Z39-18

A. Background and Motivation

A.1 Introduction

Optical measurement is central to a wide range of military and commercial applications. Leveraging the ease with which optical sensing may now be followed by sophisticated digital computing a new computational imaging (CI) paradigm has emerged in which algorithmic degrees of freedom are co-designed with the more traditional physical optical degrees of freedom to yield entirely new types of cameras. Extended depth of focus, light-field, compressive, and tomographic cameras are all examples of this new class. Unfortunately, progress in CI has been hampered by the relatively few physical degrees of freedom that are traditionally available within optical design. In this work we have sought to "open the aperture" so that a richer collection of optical degrees of freedom will be available for use within the CI paradigm. Generalized 3D index distributions have been our primary focus. Weak scattering, metamaterials, and volume holographic optical components are treated as special cases. An important goal of this work has been to identify novel design and optimization strategies that enable us to understand the relationship between 3D index distribution and optical function. A related goal has been to identify potentially useful non-image mappings (i.e., optical systems that do not attempt to replicate the object irradiance at the focal plane). For example, an ideal *digital* imager may be viewed as one in which the optical aberrations are not necessarily absent, but rather one in which the optical aberrations are computationally invertible. The CI paradigm facilitates the exploitation of these non-traditional mappings via use of joint optimization.

A.2 Computational Imaging

Imaging is Mission Critical - Optical imaging has become an important element within a wide variety of military, intelligence, homeland security, and commercial applications. It is difficult to imagine modern ISR without the advanced EO/IR imaging capabilities that we currently have at our disposal and it would be accurate to say that imaging has become ubiquitous throughout the DoD. One important driver of these capabilities has been the continuous advances in focal plane technology. [1,2] Sometimes overlooked however, is the fact that all of these impressive performance improvements have come along with another "game changing" feature – cameras are now digital. A new "computational imaging" (CI) paradigm has emerged in which algorithmic degrees of freedom may be jointly optimized along with the more traditional physical optical degrees of freedom to yield entirely new types of cameras. [3, 4] Recent demonstrations that point to the potential of this paradigm include extended depth of field imaging (i.e., in which a previously unavailable capability is enabled via joint optimization), compressive imaging (i.e., through which reductions in sensor resources and improvements in image quality are possible), and 3D imaging using the light field camera.[5-7] Unfortunately, progress in this domain has been limited by the optical degrees of freedom that are traditionally available to optical design: namely glass type, surface curvature/form, and working distances. One important goal of the work proposed here therefore will be to "open the aperture" on optical design so that a richer collection of optical degrees of freedom will be available for use within the CI paradigm.

Open the Aperture on Optical Design – Until recently cameras did not employ focal planes or digital processing. These early cameras were therefore required to generate images in a format that could be directly consumed by a human viewer. It has been convenient that simple spherical surfaces can be easily fabricated and will do a reasonably good job of forming images. For this reason most of our effort in the domain of "optical design" (OD) has been directed toward fixing the imperfections (i.e., aberrations) that arise when we attempt to employ surfaces between air and various types of glass/plastic to form images. As a result of this historic convenience and despite extraordinary progress in FPA technology, imaging optics and the associated OD activities haven't really changed much over the past several hundred years. The OD community has spent most of its intellectual energy and design resources focused on a very narrow region of optical design space near the "identity map." What this means is that the optical components in a camera (i.e., whether a low cost cell phone camera or a space telescope) are generally designed to invert the effect of propagation. The goal of these optical systems is to create an identity map between the object space and the image space. The entire study of aberration theory is an investigation into the *error* that we incur while trying to realize the identity map - essentially ignoring all of the other potentially useful mappings that could be realized.

In order to make the previous assertion a bit more rigorous consider figure 1a in which a conventional incoherent optical imaging system is depicted. The operation of this system is well-approximated by the linear mapping $g(x,y,z,\lambda) = \iiiint f(x',y',z',\lambda') \, h_n(x,y,z,\lambda,x',y',z',\lambda') \, dx'dy'dz'd\lambda'$, where $f(x,y,z,\lambda)$ is the object space irradiance distribution, $g(x,y,z,\lambda)$ is the image space (i.e., measurement space) irradiance distribution, and $h_n(x,y,z,\lambda,x',y',z',\lambda')$ is the kernel of the linear operator that results from a specific "optical configuration" (i.e., specific choices for the optical components and distances). We may capture any such optical configuration in the 3D index distribution $n(x,y,z,\lambda)$. Note that traditional OD will write $h_n(x,y,z,\lambda,x',y',z',\lambda') = \delta(x-x',y-y',z-z',\lambda-\lambda') + a(x,y,z,\lambda,x',y',z',\lambda')$ and focus most of its design efforts to minimize the aberration function $a(x,y,z,\lambda,x',y',z',\lambda')$ over some range of the object space X, Y, Z, and Λ. For notational simplicity it will sometimes be convenient to consider the input and output irradiance distributions as vectors in spaces determined by an appropriately selected basis for sampling the underlying continuous functions. [8] We will represent these object and measurement vectors as **f** and **g** respectively and note that the integral transformation above may be written as a matrix transformation between these discrete spaces as **g** = **H$_n$f**. As discussed above, conventional optical design strives to achieve **H$_n$** = **I**, the identity map, by minimizing the norm of the aberration operator **A**.
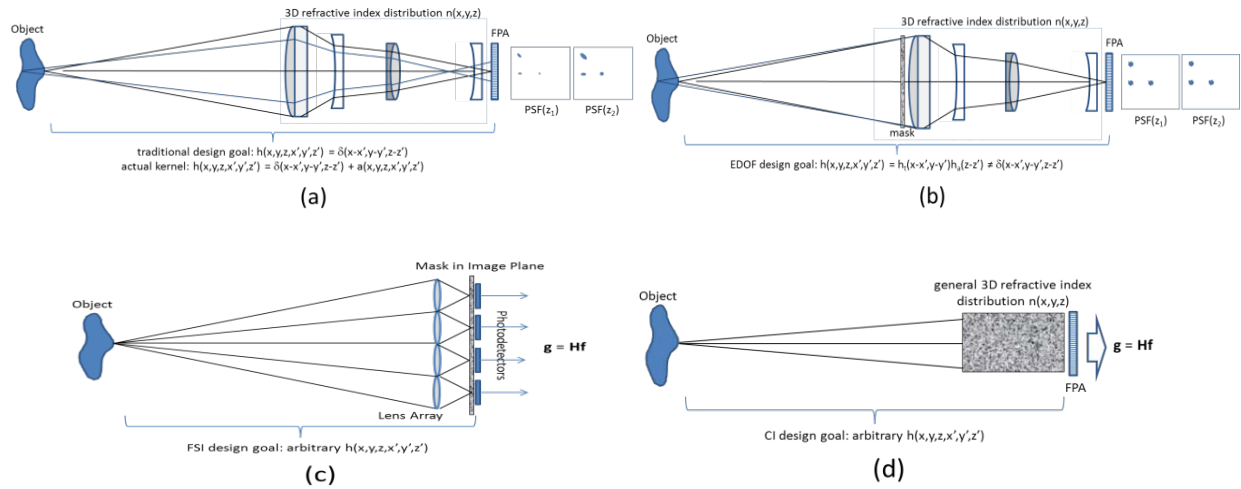

Figure 1: The evolution of optical sensing architectures. (a) Traditional imaging employs complex optical systems in order to approximate the identity operator. (b) Extended depth of field imaging employs a pupil plane mask in order to yield a more general Toeplitz operator and provide additional functionality when combined with digital post-processing. (c) Feature-specific imaging offers a more general class of system operator but requires an intermediate image. (d) Generalized 3D index distributions offer the potential to realize a much larger class of optical transformations which when jointly optimized with computational degrees of freedom will yield improved performance and reduced SWaPC.

Although it is understandable from whence this focus on the identity map derives, the advent of digital imaging and the potential for substantial post-measurement processing has expanded the landscape of OD. We are motivated to pursue designs in this broader space because (a) optical components continue to represent the dominant mass and volume costs in most cameras and (b) isomorphic image space representations (i.e., pixels) are redundant and so make sub-optimal use of photon, noise, and electrical power resources. We seek to substantially improve both performance and SWaP by noting that a FPA need not measure a pretty picture – it only has to measure the *information* required for the post-processing algorithm to succeed. This insight together with recent advances in optical fabrication (e.g., aspheric surfaces, non-rotationally symmetric surfaces, 3D GRIN optics, and metamaterials) have made possible the study of optical systems that do not strive to implement the identity map. A natural evolution has recently taken place within the CI community. The first step has been to generalize traditional lens systems (i.e., which strive to achieve the identity mapping **H$_n$=I**) to include various thin transparencies (i.e., masks). When a mask is implemented in the pupil of an optical system a more general Toeplitz or convolutional mapping (**H$_n$=H$_T$**) is realized. The extended depth of field (EDOF) camera is an example of this simple form of CI. [5, 9]

The next step in the evolution of CI has been to relax the shift-invariant property that emerges from these Toeplitz mappings and seek optical techniques for realizing more general shift-variant mappings. Ideally, these systems would fully generalize OD, enabling any arbitrary $\mathbf{H_n}$ allowed by the laws of physics. We are not there yet, but a recent step in this direction is represented by the compressive or feature-specific imaging (FSI) system shown in figure 1c. [12-15] Once again this system employs a simple mask; however, by placing this mask in an intermediate image plane, FSI is capable of realizing any positive-valued energy-conserving mapping in the transverse kernel. So the system operator for this system, $\mathbf{H_{FSI}}$ derives from a kernel of the form $h_n(x,y,z,x',y',z') = h_t(x,y,x',y')h_a(z,z')$ where $h_t(x,y,x',y')$ may be any transverse kernel allowed by physics and $h_a(z,z')$ is constrained by the imaging optics as it would be in a traditional design. In the transverse plane therefore we obtain $\mathbf{g} = \mathbf{H_{FSI}f}$, where the operator $\mathbf{H_{FSI}}$ realizes nearly-arbitrary projections of the object space. By virtue of making nearly-arbitrary measurements on the transverse irradiance distribution, FSI has been shown to offer advantages in both image quality (e.g., in high noise environments via the multiplexed advantage) and task-specific performance (e.g., via removal of confounding variables and noise). As in the case of EDOF we find that a willingness to admit solutions in which $\mathbf{H_n} \neq \mathbf{I}$ has opened the aperture in OD space to yield performance capabilities that would otherwise not be possible.

The FSI system in figure 1c may be viewed as an existence proof of both the physical realization and the potential performance advantage of a fully general optical transformation. The current approach to FSI represents an important step in the evolution of CI but suffers from two shortcomings: (a) it is hardware inefficient due to the use of reimaging optics and (b) it has not been extended to allow for programming of the axial or spectral kernels. These two issues will form a starting point for the work proposed here. A central question that we will address is: can fully general optical maps be realized without reimaging (i.e., using a simple optical device with non-traditional surfaces and/or volumetric index distribution)? A system concept for fully general optical measurements is shown in figure 1d and employs a fully general 3D index distribution. Note that all of the systems discussed thus far (i.e., figures 1a-1c) can be represented as 3D index distributions of a very limited class; those index distributions that can be generated using homogeneous materials separated by slowly-varying surfaces. It is not currently known what additional benefits may be gained via use of more general 3D index distributions and an important goal of the work proposed here will be to characterize the types of mappings that can and cannot be realized via such fully 3D optical systems. The CI paradigm enables the exploitation of these alternate mappings via use of joint optimization of optical and algorithmic variables. The overarching theme therefore is to investigate non-image-forming optical systems in conjunction with sophisticated post-processing in order to realize *system-level functionality* (e.g., either image reconstruction to form a pretty picture OR task-specific functionality that may not require such a conventional representation at any point within the processing chain) that is superior to that of a conventional camera.

B. Research Progress and Results

B.1 - Task 1: Develop a unified formalism for the analysis of optical imaging systems as general linear mappings.

This task has focused on developing design and analysis tools which will quantify the connection between a given 3D index distribution and the associated linear operator that acts between object and measurement spaces. We have pursued two main thrusts: (a) Linearized Design via Weak Scattering and (b) Multi-Linear Operators in Strong Scattering.

B.1.a Linearized Design via Weak Scattering

This section describes a method of using the first Born approximation to model the propagation of light through a weakly scattering gradient index (GRIN) medium the index of refraction of which is invariant along the optical axis. It is based on the more rigorous split step Fourier method.

Split-Step Fourier Method

In the split-step Fourier method, the optical axis in the GRIN medium is divided into N_M steps, of distance Δz. For each z position, $\boldsymbol{E}^{(m)}$, an array of length N_x, models the field distribution. The nth element in the array is the

complex amplitude of the field at the position $x = \boldsymbol{x}[n] = \Delta x \left(n - \frac{N_x+1}{2}\right)$, $z = m\Delta z$, where Δx is the spacing between samples in the x dimension. The input light field array, at $z = 0$, is given, and each subsequent light field +-array is computed based on the previous one. For each step, to simulate the light field's propagation over it, two operations are performed on the previous step's array:

$$\boldsymbol{E}^{(m)} \approx (\Delta N_m \circ P_{\Delta z})\boldsymbol{E}^{(m-1)} \tag{1}$$

The first operator, $P_{\Delta z}$, is a discrete implementation of the Fresnel diffraction integral over the distance Δz:

$$P_{\Delta z}[m,n] = \frac{e^{i\bar{n}k_0\Delta z}}{e^{i\frac{\pi}{4}}\sqrt{\lambda\Delta z}} e^{i\pi(x[m]-x[n])^2/(\lambda\Delta z)}\Delta x_m \tag{2}$$

where $\bar{n}$ is the nominal value of the index of refraction; λ is the wavelength of the light; and $k_0 = 2\pi/\lambda$. The second operator, ΔN_m, accounts for the scattering. It is the diagonal matrix such that:

$$\Delta N_m[n,n] = e^{ik_0\Delta z \boldsymbol{\delta n_m}[n]} \tag{3}$$

where the index of refraction at the coordinates $(z,x) = (m\Delta z, n\Delta x)$ is $\bar{n} + \boldsymbol{\delta n_m}[n]$. Consequently, the field distribution at the output of the GRIN medium can be expressed as a function of the input light field to the GRIN medium as follows:

$$\boldsymbol{E}^{(N_M)} = \Delta N_{N_M} \circ P_{\Delta z} \circ \Delta N_{N_M-1} \circ P_{\Delta z} \circ \ldots \circ \Delta N_1 \circ P_{\Delta z}\boldsymbol{E}^{(0)} \tag{4}$$

Weak Scattering Approximation

If the index of refraction in the GRIN is invariant in the z dimension, then:

$$\Delta N_1 = \cdots = \Delta N_{N_M} = \Delta N \tag{5}$$

$$\Rightarrow \boldsymbol{E}^{(N_M)} = (\Delta N \circ P_{\Delta z})^{N_M}\boldsymbol{E}^{(0)} \tag{6}$$

Let $M \equiv (\Delta N \circ P_{\Delta z}) - I$, where I is the identity matrix. Then:

$$\boldsymbol{E}^{(N_M)} = (I + M)^{N_M}\boldsymbol{E}^{(0)} = \sum_{m=0}^{N_M} \binom{N_M}{m} M^m \boldsymbol{E}^{(0)} \tag{7}$$

The weakly scattering approximation might be made if $\|M\| \ll 1$. In this approximation, only the first two terms of the summation are used to compute the field at the output of the GRIN:

$$\boldsymbol{E}^{(N_M)} \approx (I + N_M M)\boldsymbol{E}^{(0)} \tag{8}$$

Example: GRIN Lens

The example of a GRIN lens is used to illustrate the validity and limitations of this weakly scattering approximation. The GRIN lens has an index distribution that is a function of x:

$$n(x) = \bar{n} - \frac{x^2}{2fL_z} \tag{9}$$

where f is the back focal distance, and L_z is the thickness of the GRIN lens along the z dimension. Hence

$$\boldsymbol{\delta n_m}[n] = -\frac{\boldsymbol{x}[n]^2}{2fL_z} \forall m \tag{10}$$

Upon substitution of (10) into (3),

$$\Delta N[n,n] = e^{-ik_0\frac{x[n]^2}{2fN_M}} \tag{11}$$

If the lens is very thin, and $P_{\Delta z} \approx I$, then the split-step Fourier method calculates that the field at the rear face of the GRIN lens is $\boldsymbol{E}^{(N_M)} = \Delta N^{N_M}\boldsymbol{E}^{(0)}$. If $\boldsymbol{E}^{(0)}$ represents a normally incident plane wave, i.e.

$$\boldsymbol{E}^{(0)}[n] = 1 \ \forall \ n \tag{12}$$

then the field emerging from the lens is a spherical wave that will converge a distance f behind the lens:

$$\boldsymbol{E}^{(N_M)}[n] = e^{-ik_0\frac{x[n]^2}{2f}} \tag{13}$$

(If the lens is thicker, the back focal length can be found using Gaussian reduction, treating each of the cross sections as a thin lens with focal length $N_M f$).

Meanwhile, the weakly scattering approximation calculates the field at the rear face of the GRIN lens to be:

$$\boldsymbol{E}^{(N_M)} \approx (I + N_M M)\boldsymbol{E}^{(0)} = \boldsymbol{E}^{(0)} + N_M \Delta N \boldsymbol{E}^{(0)} \tag{14}$$

Therefore, if the field incident on the front face of the lens is the normally-incident plane wave described by (12), the weakly scattering approximation computes:

4

$$\Rightarrow \boldsymbol{E}^{(N_M)}[n] = 1 + N_M e^{-ik_0 \frac{x[n]^2}{2fN_M}} = 1 + N_M e^{-i\theta[n]}$$

<div align="right">(15)</div>

where $\boldsymbol{\theta}[n] = k_0 \frac{x[n]^2}{2fN_M}$. The greatest neglected term of the expansion in (7) is $\binom{N_M}{2} \Delta N^2 \boldsymbol{E}^{(0)}$, the *n*th component of which, given (12), is $\binom{N_M}{2} e^{-i2\theta[n]}$. So, for instance, in the case where $N_M = 2$, in order for this weakly scattering approximation to yield accurate results for the field at the rear of the GRIN lens:

$$\left| e^{-i2\boldsymbol{\theta}[n]} \right| \ll 1 \Leftrightarrow 2\boldsymbol{\theta}[n] < \frac{\pi}{4} \Leftrightarrow |x[n]| < \frac{\sqrt{\lambda f}}{2}$$

<div align="right">(16)</div>

For example, Figure 1a and Figure 1b plot fields computed with the split-step Fourier method and with the weak scattering approximation for the case where $N_M = 2, \lambda = .5\mu m, f = 3m$. As predicted by (16), the Born approximation (weakly scattering) calculations agree with the split-step Fourier calculations when $|x| < .6mm$. Figure 2 plots the amplitudes of the two computed fields of Figure 1 after an operator has been applied to them to implement the Fresnel diffraction integral to propagate them 3 m to the focal plane: The weak scattering approximation is "noisier," due to the loss of the higher order term.
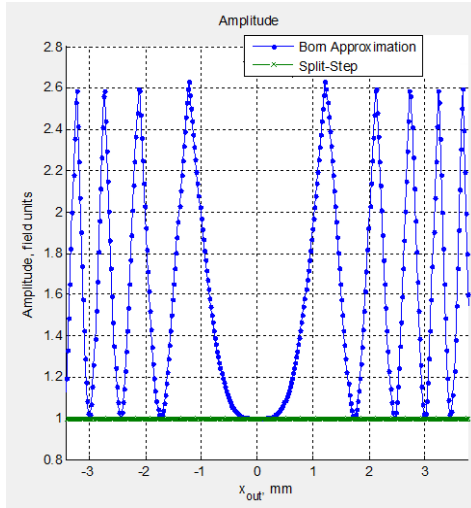
Figure 1A: $\left| \boldsymbol{E}^{(2)} \right|$ computations with split-step Fourier method and with weak scattering approximation
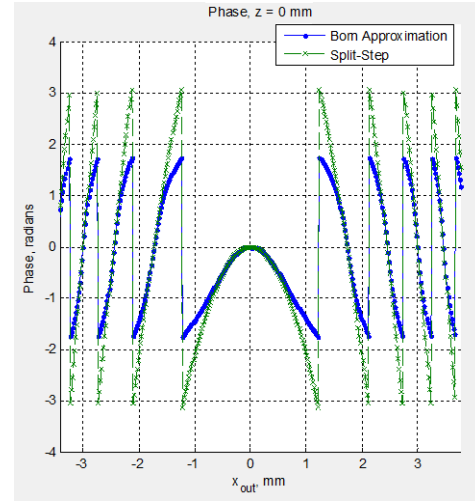
Figure 1b: $\angle \boldsymbol{E}^{(2)}$ computations with split-step Fourier method and with weak scattering approximation
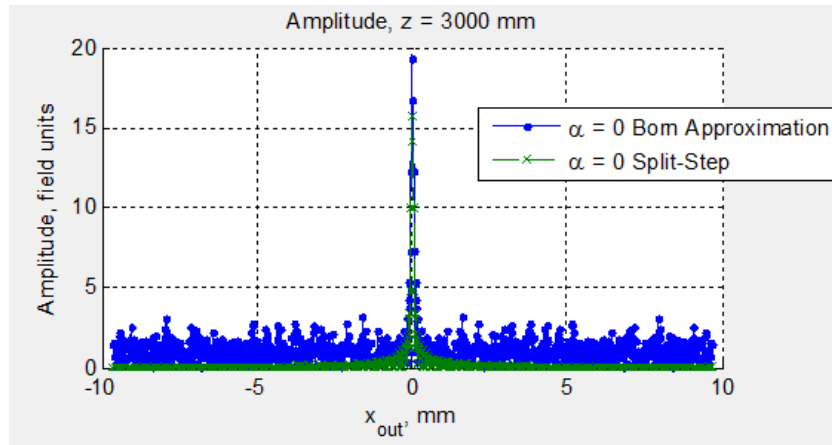
Figure 2: Fields at Rear of GRIN Lens Propagated to the Focal Plane

B.1.b Multi-Linear Operators in Strong Scattering

This sub-task treats a gradient index (GRIN) medium in the shape of a rectangular prism. The objective of this work is to find the index distribution of the GRIN medium such that a certain set of input light fields, incident on the front face, emerge from the rear face matching as closely as possible to a set of corresponding desired output light fields. In order to find this index distribution, a gradient descent algorithm is used. For each iteration of the gradient descent algorithm, the split-step Fourier method is used to model the propagation of the specified input fields through the medium and compute the distribution of the light fields at the rear face of the medium. The output light field distributions are compared with the desired output light fields, and a cost metric is calculated as a measure of how closely the realized outputs are to the desired ones. Based on the gradient of this cost metric with respect to variables that are directly related to the index of refraction distribution, the index of refraction of the medium is iteratively updated.

The Split Step Fourier Method

The split-step Fourier method, illustrated in Figure 1, is used to simulate the propagation of the light fields through the GRIN material. This method of "beam propagation" can accurately, model strong volumetric scattering. An $N_y \times N_x$ matrix U_{in} represents discrete spatial samples of an input field, in the plane $z = 0$. For the analysis, this matrix is up-sampled initially by a factor of N_O, and yielding an $N_{yo} \times N_{xo}$ matrix U_{0-}, where $N_{xo} = N_O N_x$, and $N_{yo} = N_O N_y$. U_{0-} is also scaled so that it has the same norm as U_{in}. The optical axis through the GRIN material is divided into N_M small steps of distance d. For each step, two operations are performed on this field matrix, to simulate the field's propagation over the step. First, to account for the effect of deviations in the index from the nominal value, each value of the field matrix is multiplied by a unit-amplitude complex number.

$$U_{m+}[n_y, n_x] = M_m[n_y, n_x] \times U_{m-}[n_y, n_x] \tag{17}$$

where U_{m-} is the field matrix in the plane $z = md$; U_{m+} is the updated field matrix; and M_m is an $N_{yo} \times N_{xo}$ "mask" matrix of unit-amplitude complex numbers:

$$M_m[n_y, n_x] = \exp(i\theta_m[n_y, n_x]) \tag{18}$$

The phase delays θ_m model the effect of the deviations in the index of refraction from the nominal value in the plane $z = md$. The second operation performed to simulate the field's propagation over a step is a discrete approximation of the Fresnel diffraction integral.

$$U_{(m+1)-} = \beta P U_{m+} Q \tag{19}$$

where U_{m+} is the field matrix after each element has been multiplied by the corresponding element in the "mask" matrix; and $U_{(m+1)-}$ is the new field matrix describing the field in the x-y plane for $z = (m+1)d$. The scalar β is:

$$\beta = \frac{e^{ikd}}{i\lambda d} \Delta x \Delta y \tag{20}$$

where Δx is the x-spacing of the oversampled field matrices; Δy is the y-spacing of the oversampled field matrices; λ is the wavelength; and k is the wavenumber, $\frac{2\pi}{\lambda}$, where λ is the wavelength corresponding to the nominal index of refraction. P is the $N_{yo} \times N_{yo}$ matrix such that:

$$P[n_y', n_y] = e^{i\frac{k}{2d}\Delta y^2(n_y'-n_y)^2} \tag{21}$$

Q is the $N_{xo} \times N_{xo}$ matrix such that:

$$Q[n_x', n_x] = e^{i\frac{k}{2d}\Delta x^2(n_x'-n_x)^2} \tag{22}$$

This operation is a discrete approximation of the Fresnel diffraction integral. Upon substitution of (4), (5), and (6) into (3):

$$U_{(m+1)-}[n_y', n_x'] = \frac{e^{ikd}}{i\lambda d}\Delta x \Delta y \sum_{n_y=1}^{N_y} e^{i\frac{k}{2d}\Delta y^2(n_y'-n_y)^2} \sum_{n_x=1}^{N_x} U_{m+}[n_y, n_x] e^{i\frac{k}{2d}\Delta x^2(n_x'-n_x)^2} \tag{23}$$

6

Rearrangement of (7) yields:

$$U_{(m+1)^-}[n_y', n_x'] = \frac{e^{ikd}}{i\lambda d} \sum_{n_y=1}^{N_y} \sum_{n_x=1}^{N_x} U_{m^+}[n_y, n_x] e^{i\frac{k}{2d}\left[\Delta x^2(n_x'-n_x)^2 + \Delta y^2(n_y'-n_y)^2\right]} \Delta x \Delta y \tag{24}$$

Therefore, $U_{(m+1)^-}[n_y', n_x']$ is a discrete approximation of the Fresnel diffraction integral:

$$U_{(m+1)^-}(n_x'\Delta x, n_y'\Delta y) = \frac{e^{ikd}}{i\lambda d} \iint_{-\infty}^{\infty} U_{m^+}(\xi, \eta) e^{i\frac{k}{2d}\left[(n_x'\Delta x - \xi)^2 + (n_y'\Delta y - \eta)^2\right]} d\xi d\eta \tag{25}$$
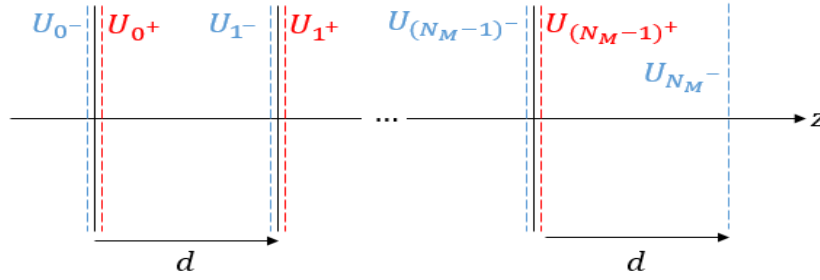

Figure 3: Split Step Fourier Method

The goal of this optimization is to find the phases of the "mask" matrices, $\theta_m[n_y, n_x]$ for $1 \le m \le N_m$, $1 \le n_y \le N_y$, $1 \le n_x \le N_x$ that minimize the difference between the field matrices that the system outputs when the specified input field matrices are sent through it, and the desired output field matrices.

The Gradient Descent Algorithm

Each iteration of the gradient descent algorithm, the phases of the masks are updated:

$$\theta_m^{(k+1)}[n_y, n_x] = \theta_m^{(k)}[n_y, n_x] - \eta \nabla_{\theta_m} cost[n_y, n_x] \tag{26}$$

where $\theta_m^{(k)}[n_y, n_x]$ is the element in row n_y and column n_x of θ_m on the kth iteration; $\theta_m^{(k+1)}[n_y, n_x]$ is the element in row n_y and column n_x of θ_m on the $k+1st$ iteration; $\nabla_{\theta_m} cost[n_y, n_x]$ is the partial derivative of the cost metric with respect to $\theta_m[n_y, n_x]$; and η is a scale factor.

The cost function used by the gradient descent is a weighted combination of the squared error between the desired and realized outputs, and a function of the correlation between the desired and realized outputs. Let $U_{out}^{(n)}$ denote the output field matrix realized by applying the split step Fourier propagation method to the nth specified input field matrix, and let $U_{out,des}^{(n)}$ be the desired output. Then the cost associated with the nth input/output pair is:

$$cost^{(n)} = \lambda_1 \times trace\left(\left(U_{out,des}^{(n)} - U_{out}^{(n)}\right)^\dagger \left(U_{out,des}^{(n)} - U_{out}^{(n)}\right)\right) + \lambda_2 \rho \tag{27}$$

where

$$\rho = -\log\left(\frac{\left|trace(U_{out}^{(n)\dagger} U_{out,des}^{(n)})\right|^2}{trace(U_{out,des}^{(n)\dagger} U_{out,des}^{(n)}) \times trace(U_{out}^{(n)\dagger} U_{out}^{(n)})}\right) \tag{28}$$

and where λ_1 and λ_2 are weights. The total cost for one iteration is the cost averaged over the N_{IO} specified input/output pairs.

$$cost = \frac{\sum_{n=1}^{N_{IO}} cost^{(n)}}{N_{IO}} \qquad (29)$$

Example: Simple Lens Optimization

In this example, the desired input/output field matrix pairs "point-source" input field distributions to "point-source" output field distributions, as a lens would. $N_x = N_y = 6$. The other parameters of the optimization are listed in the table below.

Table 1: Parameter Values for Simple Lens Optimization

Parameter	Value
N_x	6
N_y	6
N_O	20
λ	$.5\mu m$
d	$1mm$
N_M	6
λ_1	$.1$
λ_2	1
N_{it} (# of iterations)	1000
η	1

There are 36 specified input/output pairs. The nth input field matrix is zero everywhere, except that it is 1 in the row r and column c where $r = mod(n-1, 6) + 1$, and $c = floor\left(\frac{n-1}{6}\right) + 1$. The nth corresponding desired output field matrix is zero everywhere except in the row $7 - r$ and column $7 - c$. For instance, the 13th input/output field matrix pairs are illustrated in Figure 2.
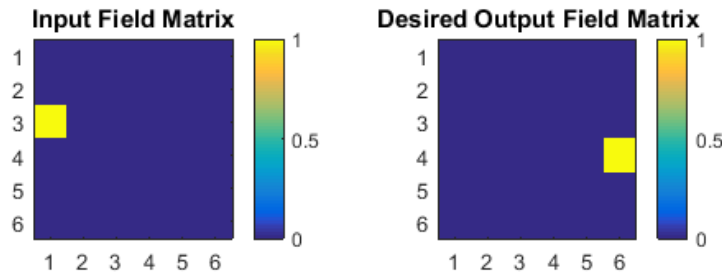

Figure 4: Simple Lens Input/Output Field Pair

These desired outputs correspond, roughly to the output fields that a simple lens would produce from the given input fields.

The optimization is run 5 different times. Each time, a different set of the "mask" matrices are allowed to be varied by the gradient descent algorithm, while the rest of the "mask" matrices are fixed at all 1's, corresponding to no deviation in the index of refraction from the nominal value. The different sets of mask matrices that are allowed to vary are listed in Table 2.

Trial	"Mask" Matrices That Are Varied
1	M_3
2	M_2, M_4
3	M_1, M_3, M_5
4	M_1, M_2, M_4, M_5
5	M_1, M_2, M_3, M_4, M_5

This experiment, furthermore, is run 8 different times, each time initializing the phases of the "mask" matrices differently. In 7 of the 8 cases, the phases of the "mask" matrices are initialized randomly, with a uniform distribution between 0 and 2π, and in the 8th case, the "vacuum-initialization" case, all phases of the "mask" matrices are initialized as 0's.

As the trial index increases, the number of free "mask" matrix parameters increases. As this number of degrees of freedom increases, it is expected that the final cost metric and the RMSE between the realized field matrices and desired field matrices decreases.

Figure 4 plots the cost metric as a function of the number of "mask" matrices being varied. Specifically, the blue curve represents the average cost of the 7 randomly-initialized trials; the orange and yellow curves represent the average cost plus or minus a standard deviation. The purple curve represents the "vacuum initialization" case. While the cost in the "vacuum initialization" case decreases monotonically with the number of varying "mask" matrices, as expected, the cost increases on average for the randomly-initialized cases.
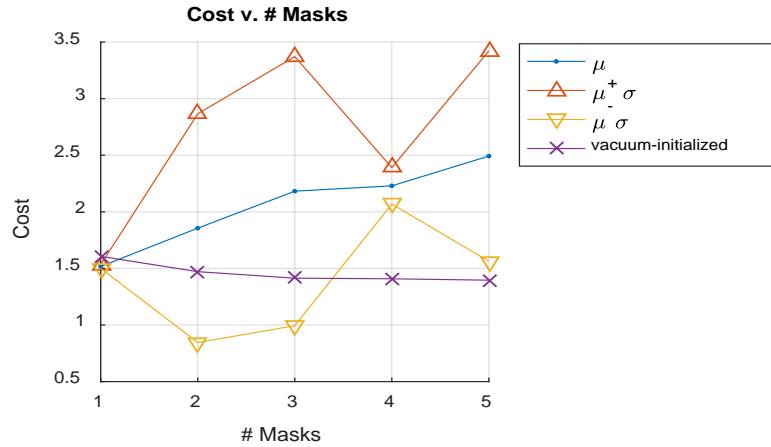

Figure 5: Cost v. # Masks

This trend is verified by Figure 4a-c, which plots $U_{out}^{(13)}$ for the vacuum initialization case with one variable "mask" matrix, for the vacuum initialization case with 5 variable "mask" matrices, for the random initialization case with one variable "mask" matrix, and for the random initialization case with 5 variable "mask" matrices. The case of random initialization case with 5 variable "mask" matrices appears worse than the others.
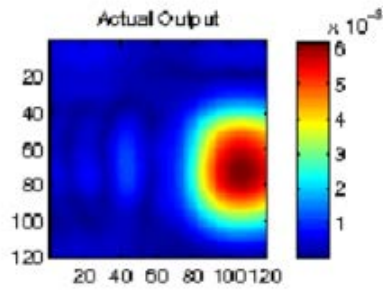
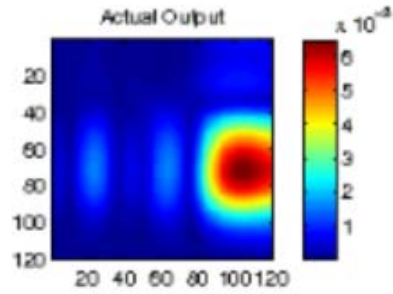Figure B.1.b.6a: $U_{out}^{(13)}$ Vacuum-Initialized, 1 mask

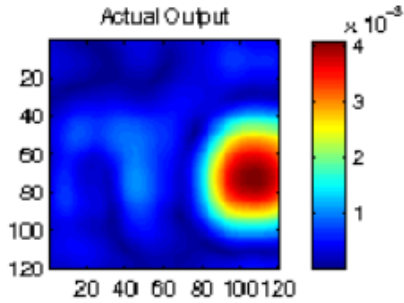Figure B.1.b.4b: $U_{out}^{(13)}$ Vacuum-Initialized, 5 masks

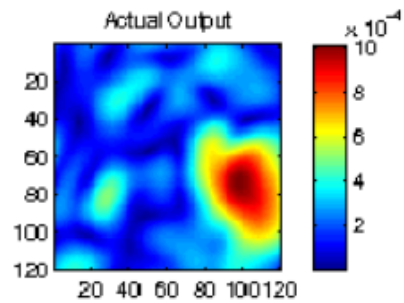Figure B.1.b.4c: $U_{out}^{(13)}$ Randomly-Initialized, 1 mask

Figure B.1.b.4d: $U_{out}^{(13)}$ Randomly-Initialized, 5 masks

Moreover, the RMSE increases with the number of free "mask" matrices. Figure 5 plots the mean RMSE, as a percentage of the dynamic range, versus the number of variable "mask" matrices. Specifically, the blue curve represents the average RMSE of the 7 randomly-initialized trials; the orange and yellow curves represent the average RMSE plus or minus a standard deviation. The purple curve represents the "vacuum initialization" case. It is hypothesized that this increase in cost and RMSE, for the randomly initialized cases, is due to an increase in local minima in the cost function as the number of "mask" matrices increases.
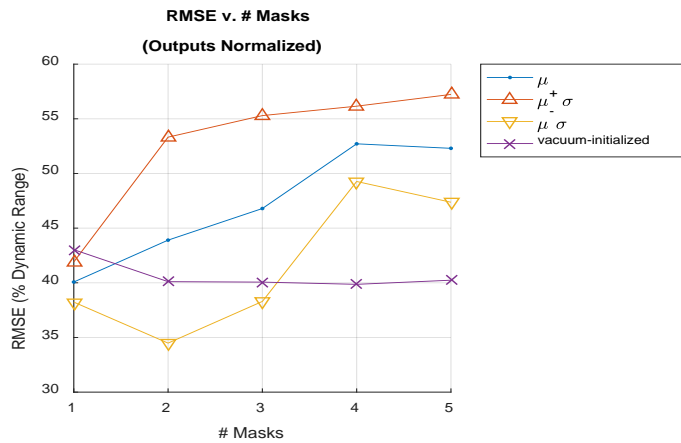

Figure 7: RMSE v. # Masks

B.2. - Task 2: Investigate volume holography (VH) as a tool for the realization of generalized non-identity optical mappings.

This task has focused on a quantitative assessment of the capabilities and limitations of VH as an optical element for the realization of arbitrary mappings. Kickoff meeting feedback from DARPA suggested that we reduce our attention to this task and as a result, we have only examined the basic 1D VH implementation of feature-specific (i.e., compressive) imaging using a few well-known projection operators.

Volume holography (VH) is used to develop a quantitative assessment of the capabilities and limitations when used as an optical element for the realization of arbitrary linear mappings. It will be almost trivial to capture the behavior (i.e., as a linear operator) of each volume grating in terms of its action on the input field, assuming "ideal" cases of unit efficiency, perfect Bragg selectivity with no crosstalk, no chromatic effect, and no degeneracy. So our task is to capture these various departures from ideality in the linear operator framework. In the computational framework, the grating dimensions or thicknesses are included as a free parameter so that the VH model scales smoothly from thin (i.e., non-Bragg) to thick (i.e., Bragg) behavior. The average refractive index n, modulation amplitude Δn, modulation vector K_g of gratings are also included as design parameters for the optics. A volume optics is suggested as a device to support a generalized class of computational imaging. In order to reveal the connection between the refractive index (RI) distribution n(x,y,z) and the system operator H, the VH is used as a functional tool to analyze/characterize the imaging performance of RI distribution. The RI distribution is linearly decomposed by volume holographic modulation

$$n(x,y,z) = \sum_{q=1}^{M} N(q) \cdot e^{-i\vec{K}_g^{(q)}\vec{r}},$$

where N is the coefficient of the VH modulation and q is the number of grating. Note the sinusoidal expansion of RI distribution can apply the diffraction theory to each component and characterize the diffraction properties of the optics. Since any smooth function can be written as a superposition of sinusoids, so both of these pictures are correct but we need to be careful which picture is physically relevant. For example, when the gratings have high spatial frequency then diffraction is the dominant effect. In the other case, ray tracing is most relevant to understand the functionality of the optics. The VH grating produces a small phase modulation to the dielectric constant ε. The magnitude of the spatial modulation ε_1 is much smaller than the average magnitude ε and the modulation direction and period is determined by the grating vector K_g. The total spatial modulation ε_T is expressed by summing up the phase distribution of the multiple gratings with an index k.

$$\varepsilon_T = \sum_k^{M} \varepsilon_{0k} + \varepsilon_{1k} \cdot \cos(\vec{K}_{gk} \cdot \vec{r}),$$

where r indicates the spatial position vector. Grating modulation is defined by the finite extent with modulations in the 3D space coordinates (x,y,z)

$$n(x,y,z) = \Delta n \operatorname{Rect}(\frac{x}{L_x}) \operatorname{Rect}(\frac{y}{L_y}) \operatorname{Rect}(\frac{z}{L_z}) e^{-i\vec{K}_g\vec{r}},$$

where Δn is the modulation amplitude in the medium and the exponential term is the grating modulation with the grating vector K_g. To simplify the efficiency model of volume hologram, we start with the 1D grating with infinite extents in the other dimensions. The 1D grating uncertainty is obtained by Fourier transforming the RI modulation. Assuming the infinite extents in the other dimensions, we ignore the Bragg condition. Because of the finite extent in the dimension, the uncertainty is side-lobed by the Sinc function which determines the diffraction distribution in the imaging range.

$$\tilde{n}(\Delta\vec{K}) = \Delta n L \operatorname{Sinc}(\frac{\vec{K} - \vec{K}_d}{2\pi/L}),$$

The diffraction distribution of volume grating is characterized by the Bragg condition and the grating uncertainty in the FOV. The grating vector is determined by the incident field vector K_I and the diffraction field vector K_D for a single grating case $K_G = K_D - K_I$. In ideal thick holograms, the Bragg condition is only possibility to diffract the light through the hologram medium. In practice, we have a range of incident fields with the vector K_i and the grating uncertainty relaxes the Bragg condition. The diffraction field vector K_d is determined by the grating vector K_G and the incident field vector K_i as shown in Fig. 2.

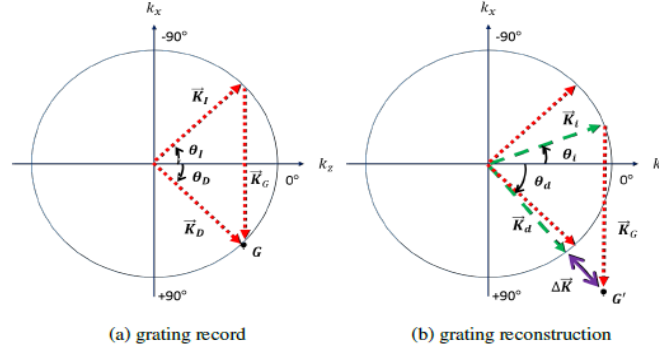(a) grating record   (b) grating reconstruction

Fig. 2: Bragg mismatch in k-space

At the incident and diffraction fields, the Bragg mismatch ∆K is estimated by the k-space distance from the point G' to the Bragg circle. The Bragg mismatch directly affects the side-lobes of the Sinc() function.

$$\Delta K = |\vec{K}_{G'} - \vec{K}_d|,$$

The diffraction field with the vector K'$_G$ is determined by the Bragg selectivity in the 2D k-space in Fig. 3. Only diffraction which satisfies the Bragg selectivity in the x and z analysis practically occurs in the VH imaging. The grating uncertainty ∆K determines the efficiency bands in the 1D imaging and the grating uncertainty is parameterized by the medium thickness. Two thicknesses of 1mm and 10μm were compared to show the Bragg selection and the thinner grating showed the broader efficiency band with weaker diffraction efficiency.

(a)   (b)   (c)

(d)   (e)   (f)
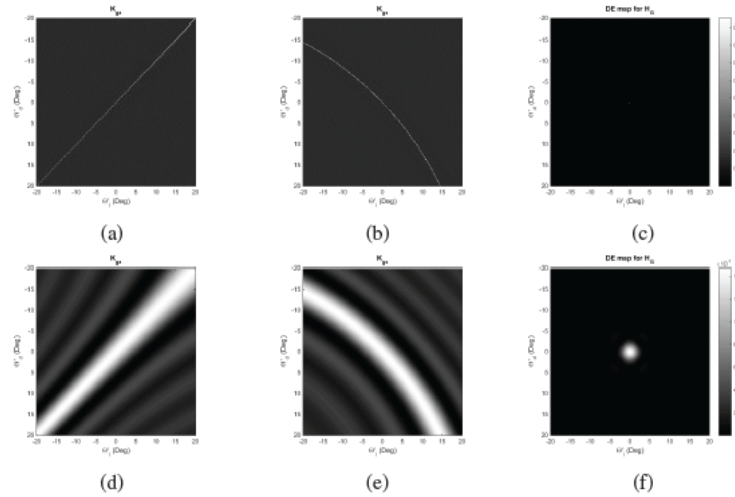
Fig. 3: Bragg selectivity in 2D k-space analysis: the grating uncertainty ΔK determines the efficiency bands in the 1D imaging and the grating uncertainty is parameterized by the medium thickness. ($1\ mm^2$ vs. $10\ \mu m^2$)

1D VH imaging is designed to show a tangible example for feature specific imaging in Fig. 4. In the operational setup, we think about object space being mapped to measurement space. Considering object space at infinity the

12

VH analysis clear to explain because the natural input modes will be plane waves and these of course will naturally arise from object points at infinity.
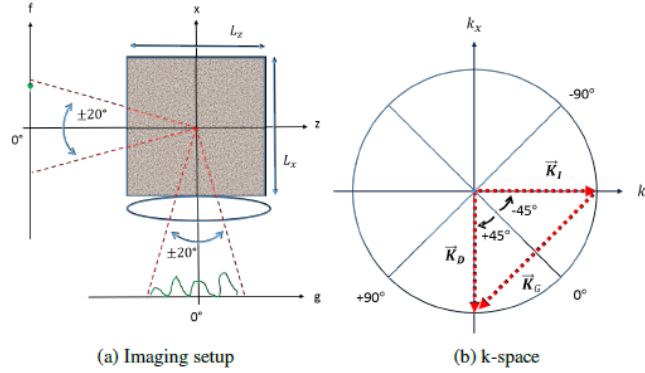

(a) Imaging setup   (b) k-space

Fig. 4: 1D VH imaging for FSI: 90 deg diffraction is the nominal mapping through the volume medium.

In the measurement space, we need a lens-like element somewhere in the volume optics (i.e., as a separate GRIN device or as a quadratic phase distortion on your gratings) to convert diffracted plane waves back to points at some finite/small distance from the GRIN. Eventually we will be interested in incoherent illumination, but for now we assume coherent but not necessarily monochromatic illumination. After the focusing lens, the grating uncertainty becomes the PSF for the system. The linear operator is defined by the shift-variant PSFs, which are characterized by Bragg selectivity and Grating uncertainty. The grating uncertainty is separately expressed in the x and z axes.

$$\tilde{n}(K_x) = \Delta n L_x \operatorname{Sinc}\left(\frac{K_x - K_{dx}}{2\pi/L_x}\right),$$
$$\tilde{n}(K_z) = \Delta n L_z \operatorname{Sinc}\left(\frac{K_z - K_{dz}}{2\pi/L_z}\right),$$

where the Bragg mismatches are denoted by $\Delta K_x = K_x - K_{gx}$ and $\Delta K_z = K_z - K_{gz}$ in the axes. The k-space distances are calculated by trigonometry in the k-space.

$$\Delta K_z = \beta(\cos\theta_i + \cos\theta_D - \cos\theta_I - \cos\theta_d),$$
$$\Delta K_x = \beta(-\sin\theta_i - \sin\theta_D + \sin\theta_I + \sin\theta_d),$$

where β is the average propagation constant and θ is the angle for the corresponding grating vectors. Diffraction efficiency is directly related to the uncertainty distance in the k-space and 1D diffraction efficiency is obtained by multiplying the individual diffraction efficiencies.

$$\eta_{1D} = \eta_x(\vec{K}_i, \vec{K}_d) \cdot \eta_z(\vec{K}_i, \vec{K}_d),$$

The RI distribution n is modeled by the linear combination of VH gratings thus the system operator H is directly defined by the characteristics of VH gratings. Once we find an ideal system matrix H_I from FSI imaging, the system performance is characterized using the VH analysis. The system matrix H_T is estimated by summing the single grating matrices H_i with proper weights w_i. Since the system matrix is optically encoded by the VH gratings, the system matrix is possible to be made by a linear combination of grating matrices H_i. The corresponding weights w_i is obtained by projecting the ideal system matrix H_I in the space of H_i. Due to the characteristics of individual gratings in the system matrix, the matrix H_T is not exactly equal to the ideal matrix H_I, which causes the performance degradation in FSI applications.

$$H_T = \sum_i^M w_i \cdot H_i,$$

$$w_i = \frac{H_i^T}{||H_i||_1} H_I,$$

$$H_I \simeq H_T + \text{error}.$$

For the system operator of FSI, we examine Hadamard, PCA, and random Bernoulli operators. The Hadamard code, composed of '-1' and '1' transmittance, is an orthogonal matrix balancing the two entry values. Using the multiplexing benefit, the MSE is reduced by a factor of 4x. The PCA code is optimum in the sense that they provide dimensionality reduction with the smallest possible MSE. The column vectors are principal components trained from 5 differently categorized images. A random Gaussian code, generated by 0 mean and 1 std, is QR factorized to make the orthogonality in columns. A random Bernoulli code, composed of '-1' and '1' transmittance, is designed by the Bernoulli distribution with 50% probability. Thus the code has the half of opening and the half of closing. In compressive sensing the system matrix H_T will not be full rank so the image reconstruction will require some prior and/or regularization. The simple matrix inversion H_{-1} is impossible, which should reduce to H_T in the noise-free case. The linear measurement model is vectorized to incorporate with a sparse optimization and we use the vectorized data of the measurement **g** and the object **f** with the designed system matrix H. The LMMSE is adopted by an optimal linear reconstruction operator depending on no free parameters and the linear operator serves as a well-defined baseline for the study. In the compressive measurement of g, the operator W is defined by the object autocorrelation matrix R and the noise covariance matrix D. The reconstruction f* is obtained by multiplying the measurement with the operator,

$$\mathbf{g} = H \cdot \mathbf{f} + \mathbf{n},$$

$$W = R \cdot H_T^T \cdot (H \cdot R \cdot H_T^T + D)^{-1},$$

$$\mathbf{f}^* \simeq W \cdot \mathbf{g},$$

where singular value decomposition is used to invert the matrix. The object autocorrelation can be obtained from training data or from one of the many popular models for natural images (i.e., the power spectrum of natural scenes). The noise covariance does not need to be trained it is diagonal (if iid noise). If the noise is AWGN then it will be proportional to the identity; whereas, if the noise is shot, then the diagonal will be proportional to the object. To decode the compressed measurement in g, the sparse optimization is used to alleviate the underdetermined problem. The system matrix H represents a highly underdetermined system, which makes the inverse problem hard. However, an optimization procedure that imposes sparsity constraints on f can return the most plausible one consistent with the given g. The sparsity constraints of compressive sensing [12, 13] turn the inverse problem into one that can be solved using, for instance, l1-minimization. The sparsity based optimization can be expressed by

$$\mathbf{f}^* = \arg\min_{\mathbf{f}} \frac{1}{2} ||\mathbf{g} - \mathbf{H} \cdot \mathbf{f}||_2^2 + \tau ||\mathbf{f}||_1,$$

where f* indicates the estimate of data from the optimization problem, and τ is a regularization parameter for the total variation term. In the computational processing, TV based TwIST algorithm was used for the inversion problem.

Five test signals were randomly chosen to represent the smooth objects in the 1D imaging scenario. Sensing rates of [5, 25, 45, 65, 85, 100] % were used to compressively reconstruct the signals with additive Gaussian noises of [no noise, 90, 30, 5] SNRs. The LMMSE optimizer was used to characterize the 1D imaging performance with four different operators in Fig. 7 and the LMMSE optimization is compared to the transpose solution of the operators in Fig. 8. The LMMSE optimization is generally superior to the transpose solution in compressive reconstruction. Looking at the LMMSE results, the ideal operators show very similar normalized root-mean-square deviations (NRMSD) with the VH operators. As the SNR increases, the

NRMSD steeply improves in general. In the case of SNR=5, the NRMSDs worsen at 100. In the numerical experiments, four system operators of Hadamard, PCA, Random Bernoulli, and Random Gaussian are tested with four optimizers of LMMSE, TV minimization, and L1 minimization. The number of resolution elements are 64 for both input and output field-of views.

The VH implementation is not much inferior to the ideal system operator in condition number and log(MSE). Now the index variation Dn is small enough not to cause a significant degradation. The results are promising, showing that the performance of the noise-free VH system can be very close to the ideal system. The x-axis indicates the sensing rate for the compressive measurement. So 100% sensing rate means 64 measurements for 64 object samples. Since optical systems cannot measure the negative values, the dual rail signal was used subtracting one positive mask with the other positive mask. The maximum absolute column sum normalization is also taken into account to preserve the photon number in the optical measurement.
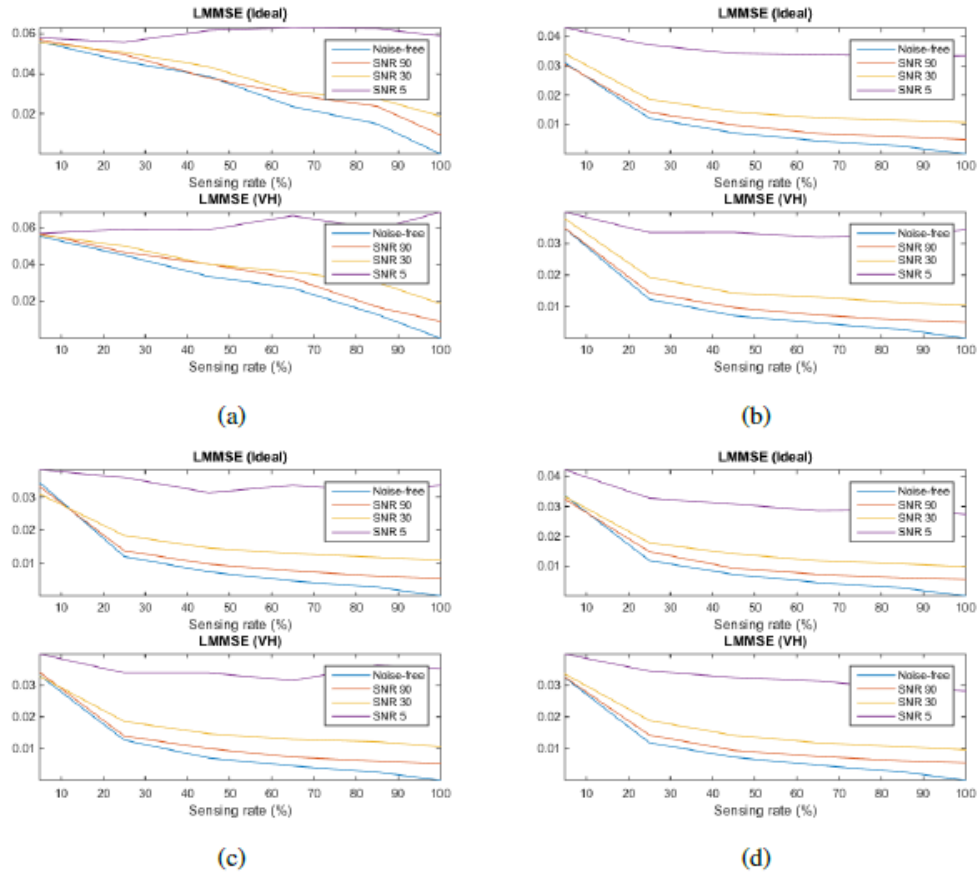

Fig. 7: LMMSE optimization for 1D imaging operators: (a) Hadamard, (b) PCA, (c) Random code with Bernoulli, and (d) Random code with Gaussian and orthogonalization.
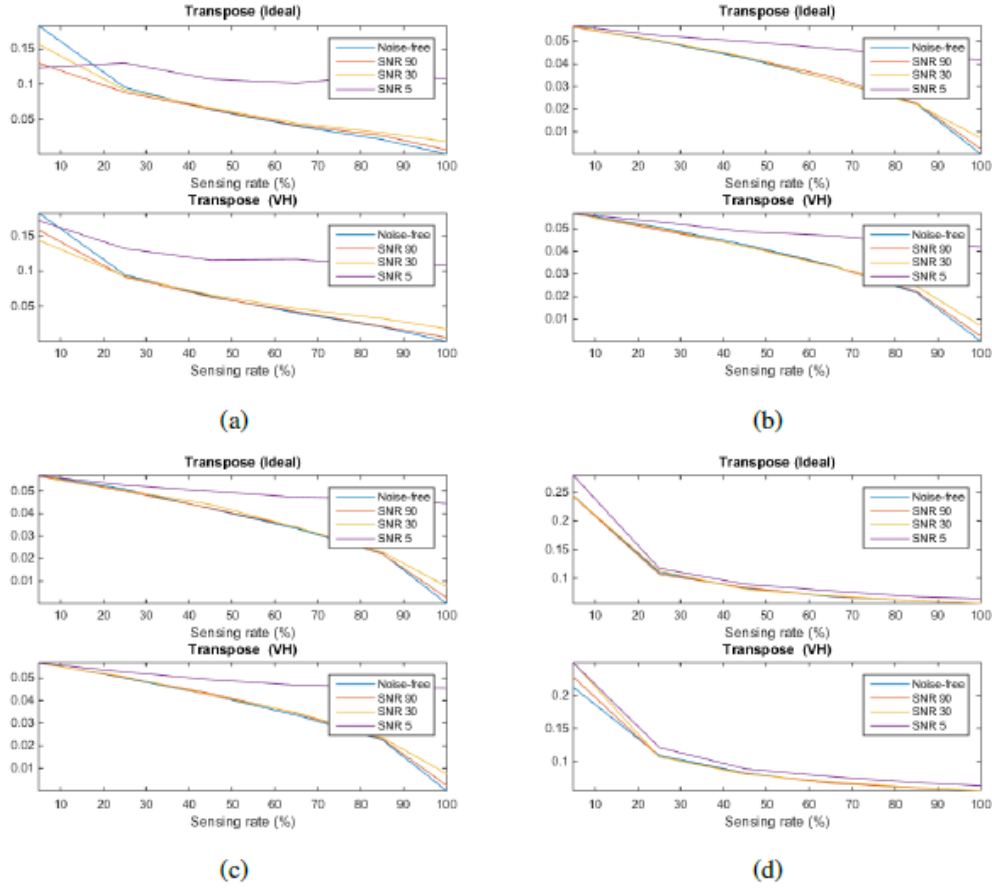
Fig. 8: Transpose for 1D imaging operators: (a) Hadamard, (b) PCA, (c) Random code with Bernoulli, and (d) Random code with Gaussian and orthogonalization.

B.3 - Task 3: Investigate the use of completely general 3D index distributions for the realization of non-identity optical mappings.

This task has been pursued in two thrusts. The first thrust has leveraged the multi-linear formulation developed in Task 1 to realize non-identity optical transforms. Because the computational complexity of the resulting optimization problem prohibits extension to high dimensions we have also pursued meta-material solutions to this class of problem. Once again in accordance with kick-off meeting DARPA feedback, we have limited our attention to identity operators in this second thrust.

B.3.a Multi-Linear Hadamard Imager

The input/output pairs are 8x8 matrices. Each of the 64 inputs is a different "point source." The corresponding desired output matrix is the output of the operator

$$H = \frac{1}{\sqrt{8}} \begin{bmatrix} +1 & +1 & +1 & +1 & +1 & +1 & +1 & +1 \\ +1 & +1 & +1 & +1 & -1 & -1 & -1 & -1 \\ +1 & +1 & -1 & -1 & -1 & -1 & +1 & +1 \\ +1 & +1 & -1 & -1 & +1 & +1 & -1 & -1 \\ +1 & -1 & -1 & +1 & +1 & -1 & -1 & +1 \\ +1 & -1 & -1 & +1 & -1 & +1 & +1 & -1 \\ +1 & -1 & +1 & -1 & -1 & +1 & -1 & +1 \\ +1 & -1 & +1 & -1 & +1 & -1 & +1 & -1 \end{bmatrix}$$

16

applied to the point source input. In all tests, there are 5 masks. The spacing between masks is $1mm$, for a total propagation distance of $5mm$. The oversampling factor is 28. The 8x8 mask pixels are spaced $10\mu m$ apart in both the x and y dimensions. The wavelength is $.5\ \mu m$. 1000 iterations were run, and two tests have finished: one in which only the center mask is allowed to vary, and the other in which all 5 masks are allowed to vary.

Figure 1a shows the intended 52nd output; Figure 1b shows the 51st output realized in the test with the single active mask; and Figure 1c shows the 51st output realized in the test with the 5 active masks. While the case with the 5 active masks yields an output closer to the intended one, neither test realized the output closely. The average RMSE between the desired output and the realized, normalized output is plotted in figure 2.
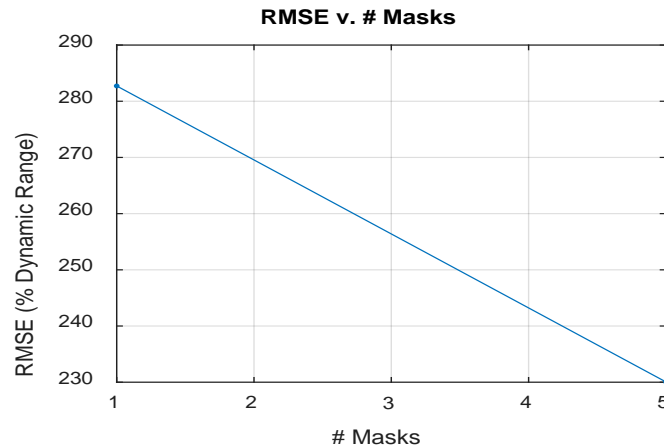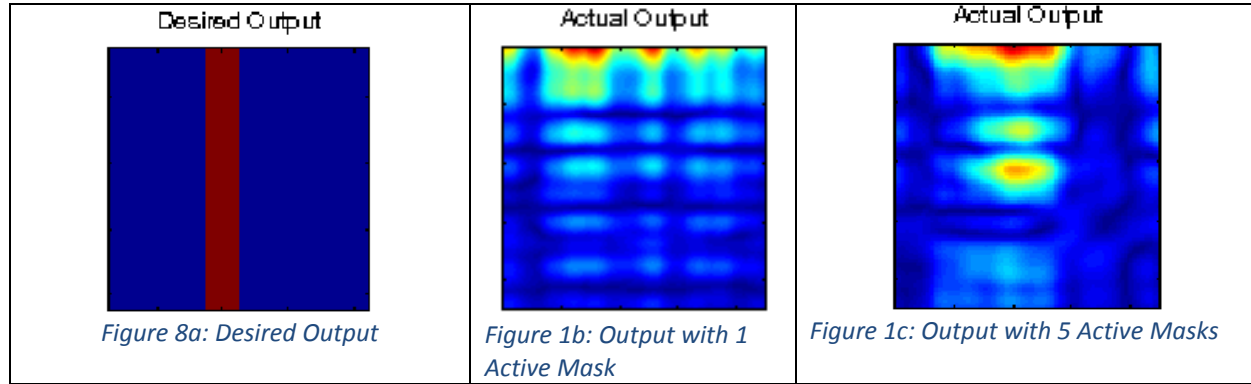
Desired Output	Actual Output	Actual Output
Figure 8a: Desired Output	*Figure 1b: Output with 1 Active Mask*	*Figure 1c: Output with 5 Active Masks*

Figure 2: Output RMSE versus number of masks for the Hadamard index distribution.

B.3.b Metamaterials Re-Imager

Quasi-conformal transformation optics, or QCTO, was invented by Li and Pendry [1] in order to yield designs that were more manufacturable. For 2-D optical systems, in which light only propagates in two dimensions, QCTO can be used to produce non-magnetic, dielectric-only material prescriptions. For cylindrically-symmetric optical systems, QCTO can be used to find material prescriptions such that the permeability tensor is non-unity only in the azimuth direction. These prescriptions are more likely to be manufacturable than general TO prescriptions, as most magnetically-coupled metamaterials provide a magnetic response in only one direction [2].

Material prescriptions that have a narrower range of constitutive parameters are also more likely to be manufacturable. This paper analyzes the effect of optimizing the shape of a concave-plano lens designed with QCTO in order to make the range of constitutive parameters as narrow as possible. QCTO is applied to Maxwell's fish-eye lens, reshaping it into a concave-plano lens that can image a curved surface onto a flat detector, as illustrated in Figure 1. Various parameters of the shape of the concave-plano lens are varied, and the effect on the range of constitutive parameters is analyzed.
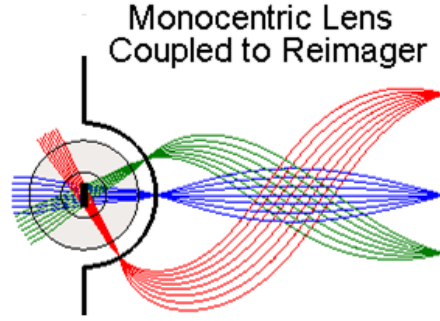

Figure 9: Monocentric Lens Coupled to a Concave-Plano Reimager. The spherical image plane of the monocentric lens is imaged onto a flat detector plane.

In Figure 1, the concave-plano lens is shown reimaging a monocentric lens. Monocentric lenses are spherically symmetric lenses that have a hemispherical image surface. Over the last several years, several promising ways to reimage the monocentric lens' curved image have been proposed and prototyped, including capturing the surface with micro-camera relays [3] and transmitting the image to a flat detector plane via fiber bundles [4]. The concave-plano reimager here would represent yet another method of reimaging the monocentric lens.
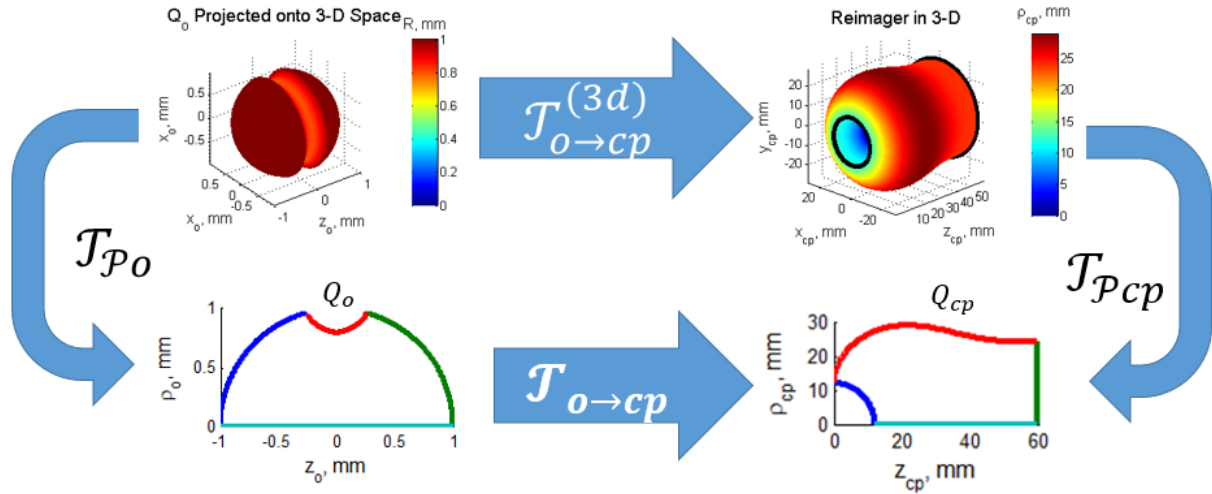

Figure 10: The relationship between the curvilinear quadrilaterals and the transformation . This figure illustrates the relationship between the curvilinear quadrilaterals and the transformation.

As illustrated in Figure 2, the transformation that reshapes Maxwell's fish-eye lens, a sphere, into a concave-plano shape is designated $\mathcal{T}_{o \to cp}^{(3d)}: U_o^{(3d)} \to U_{cp}^{(3d)}$. $U_o^{(3d)}$ and $U_{cp}^{(3d)}$ are three-dimensional spaces described by the Cartesian coordinates (x_o, y_o, z_o) and (x_{cp}, y_{cp}, z_{cp}) respectively, as well as by the cylindrical coordinates (ρ_o, ϕ_o, z_o) and $(\rho_{cp}, \phi_{cp}, z_{cp})$ respectively. The z_o- and z_{cp}- axes are the two optics' axes of symmetry. This 3-D transformation is related to the 2-D conformal transformation $\mathcal{T}_{o \to cp}: U_o \to U_{cp}$ as follows:

$$(x_{cp}, y_{cp}, z_{cp}) = \mathcal{T}_{o \to cp}^{(3d)}(x_o, y_o, z_o) \Longleftrightarrow \begin{cases} (z_{cp}, \rho_{cp}) = \mathcal{T}_{o \to cp}(z_o, \rho_o) \\ \phi_{cp} = \phi_o \end{cases} \quad (30)$$

The components of the constitutive parameter tensors then are specified by (2)-(5) [2]:

$$\varepsilon_{\rho_{cp}}(z_{cp}, \rho_{cp}) = \varepsilon_{z_{cp}}(z_{cp}, \rho_{cp}) = \varepsilon\left(\mathcal{T}_{cp \to o}(z_{cp}, \rho_{cp})\right) \times \left(\frac{\rho_o}{\rho_{cp}}\right)^2 \tag{31}$$

$$\varepsilon_{\phi_{cp}}(z_{cp}, \rho_{cp}) = \frac{\varepsilon\left(\mathcal{T}_{cp \to o}(z_{cp}, \rho_{cp})\right)}{\left|J_{o \to cp}\left(\mathcal{T}_{cp \to o}(z_{cp}, \rho_{cp})\right)\right|} \tag{32}$$

$$\mu_{\rho_{cp}}(z_{cp}, \rho_{cp}) = \mu_{z_{cp}}(z_{cp}, \rho_{cp}) = 1 \tag{33}$$

$$\mu_{\phi_{cp}}(z_{cp}, \rho_{cp}) = \frac{1}{\left|J_{o \to cp}\left(\mathcal{T}_{cp \to o}(z_{cp}, \rho_{cp})\right)\right|} \times \left(\frac{\rho_{cp}}{\rho_o}\right)^2 \tag{34}$$

In these equations, $\varepsilon_{\rho_{cp}}(z_{cp}, \rho_{cp})$, $\varepsilon_{\phi_{cp}}(z_{cp}, \rho_{cp})$, and $\varepsilon_{z_{cp}}(z_{cp}, \rho_{cp})$ are the components of the permittivity tensor in the new optic, oriented in the radial, azimuthal, and longitudinal directions respectively; $\mu_{\rho_{cp}}(z_{cp}, \rho_{cp})$, $\mu_{\phi_{cp}}(z_{cp}, \rho_{cp})$, and $\mu_{z_{cp}}(z_{cp}, \rho_{cp})$ are the corresponding components of the new optic's permeability tensor; $\varepsilon(z, \rho)$ is the isotropic permittivity of the original optic (Maxwell's fish-eye); ρ_o is the radial coordinate of the preimage of (z_{cp}, ρ_{cp}) under $\mathcal{T}_{o \to cp}(z_o, \rho_o)$; $\mathcal{T}_{cp \to o} \equiv \mathcal{T}_{o \to cp}^{-1}$; and $\left|J_{o \to cp}(z_o, \rho_o)\right|$ denotes the determinant of the Jacobian of $\mathcal{T}_{o \to cp}(z_o, \rho_o)$. Therefore, in the material described by (2)-(5), all light travelling in meridional planes, regardless of polarization, experiences a non-magnetic response with index of refraction described by (6):

$$n_{cp}(z_{cp}, \rho_{cp}) = \frac{n_o(\mathcal{T}_{cp \to o}(z_{cp}, \rho_{cp}))}{\sqrt{\left|J_{o \to cp}(\mathcal{T}_{cp \to o}(z_{cp}, \rho_{cp}))\right|}} \tag{35}$$

where $n_o(z_o, \rho_o)$ is the original index distribution in Maxwell's fish-eye:

$$n_o(z_o, \rho_o) = \frac{n_0}{1 + \dfrac{z_o^2 + \rho_o^2}{R_o^2}} \tag{36}$$

where n_0 is an arbitrarily-chosen scale factor, and R_o is the radius of Maxwell's fish-eye, which may be arbitrarily set to $1\ mm$.

In order to obtain numerical samples of the constitutive parameters of the new, reshaped lens, a discrete set of input points and corresponding output points of the conformal function $(z_{cp}, \rho_{cp}) = \mathcal{T}_{o \to cp}(z_o, \rho_o)$ are first found numerically, by way of the following methodology. Initially, two "curvilinear quadrilaterals," or closed chains of four arcs, are specified: Q_o and Q_{cp}. These two quadrilaterals are shown in Figure 2. Q_o is specified in terms of the radius of Maxwell's fish-eye, R_o, which, arbitrarily, may be set to $1\ mm$. Q_o is the image under $\mathcal{T}_{\mathcal{P}o}(x_o, y_o, z_o)$ of a closed surface that mostly aligns with the outer shell of Maxwell's fish-eye. Here, $\mathcal{T}_{\mathcal{P}o}: U_{cp}^{(3d)} \to U_{cp}$ designates the projection from $U_o^{(3d)}$ onto U_o. Similarly, $\mathcal{T}_{\mathcal{P}cp}: U_{cp}^{(3d)} \to U_{cp}$ designates the projection from $U_{cp}^{(3d)}$ onto U_{cp}:

$$\mathcal{T}_{\mathcal{P}O}(x_o, y_o, z_o) = \left(z_o, \sqrt{x_o^2 + y_o^2}\right) = (z_o, \rho_o) \tag{37}$$

$$\mathcal{T}_{\mathcal{P}cp}(x_{cp}, y_{cp}, z_{cp}) = \left(z_{cp}, \sqrt{x_{cp}^2 + y_{cp}^2}\right) = (z_{cp}, \rho_{cp}) \tag{38}$$

Hence Q_{cp} sets the shape of the reimager: it is the image of the boundary surface of the reimager under $\mathcal{T}_{\mathcal{P}cp}(x_{cp}, y_{cp}, z_{cp})$. The left arc of Q_{cp} corresponds to the concave front surface. The right line segment corresponds to the flat back detector surface. Then, with numerical grid-generation techniques, as described in [5] and [6], grid-point arrays, $(\hat{z}_o[i,j], \hat{\rho}_o[i,j])$ and $(\hat{z}_{cp}[i,j], \hat{\rho}_{cp}[i,j])$, are computed on and inside Q_o and Q_{cp} respectively, such that:

$$\mathcal{T}_{o \to cp}(\hat{z}_o[i,j], \hat{\rho}_o[i,j]) = (\hat{z}_{cp}[i,j], \hat{\rho}_{cp}[i,j]) \tag{39}$$

where $\mathcal{T}_{o \to cp}(z_o, \rho_o)$ is conformal.

Then, for each point $(\hat{z}_{cp}[i,j], \hat{\rho}_{cp}[i,j])$, an approximation of $n_{cp}(\hat{z}_{cp}[i,j], \hat{\rho}_{cp}[i,j])$ is computed with the equation:

Approved for public release: distribution is unlimited.

$$\hat{n}_{cp}[i,j] = \frac{n_0}{1 + (\hat{z}_o[i,j]/R_o)^2 + (\hat{\rho}_o[i,j]/R_o)^2} \times \sqrt{\frac{|\hat{J}_{\ell \to o}|_{i,j}}{|\hat{J}_{\ell \to cp}|_{i,j}}} \tag{40}$$

where:

$$|\hat{J}_{\ell \to o}|_{i,j} = \left\| \begin{bmatrix} \dfrac{\hat{z}_o[i+1,j] - \hat{z}_o[i,j]}{\Delta\xi} & \dfrac{\hat{z}_o[i+1,j] - \hat{z}_o[i,j]}{\Delta\eta} \\ \dfrac{\hat{\rho}_o[i+1,j] - \hat{\rho}_o[i,j]}{\Delta\xi} & \dfrac{\hat{\rho}_o[i+1,j] - \hat{\rho}_o[i,j]}{\Delta\eta} \end{bmatrix} \right\| \tag{41}$$

and

$$|\hat{J}_{\ell \to cp}|_{i,j} = \left\| \begin{bmatrix} \dfrac{\hat{z}_{cp}[i+1,j] - \hat{z}_{cp}[i,j]}{\Delta\xi} & \dfrac{\hat{z}_{cp}[i+1,j] - \hat{z}_{cp}[i,j]}{\Delta\eta} \\ \dfrac{\hat{\rho}_{cp}[i+1,j] - \hat{\rho}_{cp}[i,j]}{\Delta\xi} & \dfrac{\hat{\rho}_{cp}[i+1,j] - \hat{\rho}_{cp}[i,j]}{\Delta\eta} \end{bmatrix} \right\| \tag{42}$$

are the first order finite difference numeric approximations of $\left| J_{\ell \to o}\big(\mathcal{T}_{o \to \ell}(\hat{z}_o[i,j], \hat{\rho}_o[i,j])\big) \right|$ and $\left| J_{\ell \to cp}\big(\mathcal{T}_{cp \to \ell}(\hat{z}_{cp}[i,j], \hat{\rho}_{co}[i,j])\big) \right|$ respectively.

As long as the quadrilaterals' lateral sides are aligned with the optics' object and image surfaces, arbitrary quadrilaterals accomplish the design goal. Different quadrilaterals Q_o and Q_{cp}, however, yield different constitutive parameters. The effect of several different parameters of the quadrilaterals on the range of the refractive index is thus assessed with the following procedure. First, a particular Q_o is chosen. Then Q_{cp} is defined by a parameterized formula. The value of each Q_{cp} parameter is varied over several test trials, while the others are held fixed. For each test case, the metric $\Delta\hat{n}_{cp}^w$ is calculated, as defined in (14):

$$\Delta\hat{n}_{cp}^w \equiv \frac{\max_{(i,j)\in\mathbb{I}_\Omega} \left\{ \hat{n}_{cp}[i,j] \right\}}{\min_{(i,j)\in\mathbb{I}_\Omega} \left\{ \hat{n}_{cp}[i,j] \right\}} \tag{43}$$

$\mathbb{I}_\Omega$ in (14) denotes the set of points $\left\{ (i,j): \big(\hat{z}_{cp}[i,j], \hat{\rho}_{cp}[i,j]\big) \in \Omega^{(60)} \right\}$. $\Omega^{(60)} \subset U_{cp}$ is the set of points on and interior to Q_{cp} to which $\mathcal{T}_{\mathcal{P}cp}(x_{cp}, y_{cp}, z_{cp})$, defined in (9), projects the points inside the reimager needed to reimage a $\pm 60°$ field. $\Delta\hat{n}_{cp}^w$ is therefore the ratio of the maximum index to the minimum index. It is useful because it does not depend on the arbitrarily-chosen scale factor n_0 in (7) nor the arbitrarily-chosen radius of Maxwell's fish-eye R_o. Finally, the relationship between the Q_{cp} parameters and $\Delta\hat{n}_{cp}^w$ is used to assess the effects of the quadrilateral parameters on index range and determine the final design.

The chosen structure of Q_o is diagrammed in Figure 3. The bottom side of Q_o is the diameter of Maxwell's fish-eye lens that is on the optical axis: $\{(z_o, 0) \in U_o : |z_o| \leq R_o\}$. Meanwhile, the left and right sides are: $\{(\mp R_o \cos\theta, R_o \sin\theta) \in U_o : 0 \leq \theta \leq \varphi_o\}$, where $\varphi_o = 80°$; where the negative sign corresponds to the left side; and where the positive sign to the right side. The top side is symmetric in z_o. Each half of this symmetric top side is defined by the cubic parametric equations in (15) and (16) for $0 \leq s \leq 1$, where the top signs in the '$\mp$' and '$\pm$' correspond to the left part; and the bottom signs to the right segment. (15) specifies $z_{oT}(s)/R_o$, the ratio of the z_o-coordinate of the top side to R_o, as a function of the parameter s. (16) similarly specifies $\rho_{oT}(s)/R_o$, the ratio of the ρ_o-coordinate to R_o as a function of s. The top is configured such that it forms a 90° angle with the side, such that it is level at the midpoint, at height $h_o = .8R_o$, and, arbitrarily, such that $|z_{oT}'(0)| = \frac{1}{4} \times R_o \cos\varphi_o$.

$$z_{oT}(s)/R_o = \mp\cos\varphi_o \pm \frac{1}{4}\cos\varphi_o\, s + \left\{ \pm\frac{5}{2}\cos\varphi_o - \frac{1}{4} \right\} s^2 + \left\{ \mp 1.75\cos\varphi_o + \frac{1}{4} \right\} s^3 \tag{44}$$

$$\rho_{oT}(s)/R_o = \sin\varphi_o - \frac{1}{4}\sin\varphi_o\, s + \left\{ -\frac{5}{2}\sin\varphi_o + 3h_o \right\} s^2 + \{ 1.75\sin\varphi_o - 2h_o \} s^3 \tag{45}$$
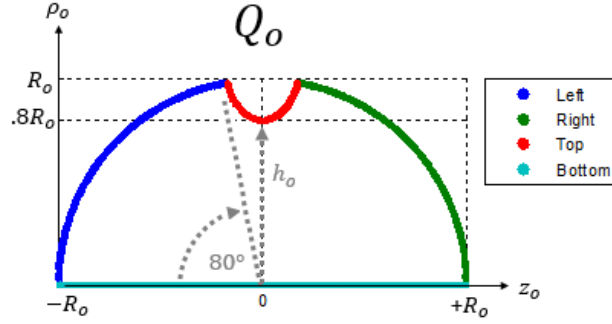
Figure 11: Q_o. The chosen structure of Q_o

While it might be useful in general to study variations in Q_o, in addition to Q_{cp}, this analysis only varies Q_{cp} parameters. For all tests, $\varphi_o = 80°$ and $h_o = .8R_o$.

For this analysis, Q_{cp} is defined with the parameters R_{cp}, W_0, ϕ, H_D, and a depicted in Figure 4. R_{cp} is the radius of the monocentric imager. Since this reimager is designed based on the monocentric lens of [7], $R_{cp} = 11.9885\ mm$. W_0, meanwhile, is the length of the reimager along the optical axis. As shown in Figure 4, the bottom side of Q_{cp} is a horizontal line segment on the z_{cp}-axis: $\{(z_{cp}, 0) \in U_{cp} : R_{cp} \leq z_{cp} \leq R_{cp} + W_0\}$. The left side, additionally, is a subset of the image, under $\mathcal{T}_{\mathcal{P}cp}(x_{cp}, y_{cp}, z_{cp})$, of the monocentric's image surface. It subtends angle $\frac{\phi}{2}$. The monocentric lens' center of curvature corresponds to the origin of U_{cp}; hence the left side is: $\{(R_{cp}\cos\theta, R_{cp}\sin\theta) \in U_{cp} : 0 \leq \theta \leq \frac{\phi}{2}\}$. $\frac{\phi}{2}$ must be at least the desired half field of view. By contrast, the right side is a straight vertical line segment of length $\frac{H_D}{2}$, where H_D is the full diameter of the flat back surface, where the detector can be placed. It is the set $\{(R_{cp} + W_0, \rho_{cp}) \in U_{cp} : 0 \leq \rho_{cp} \leq \frac{H_D}{2}\}$.
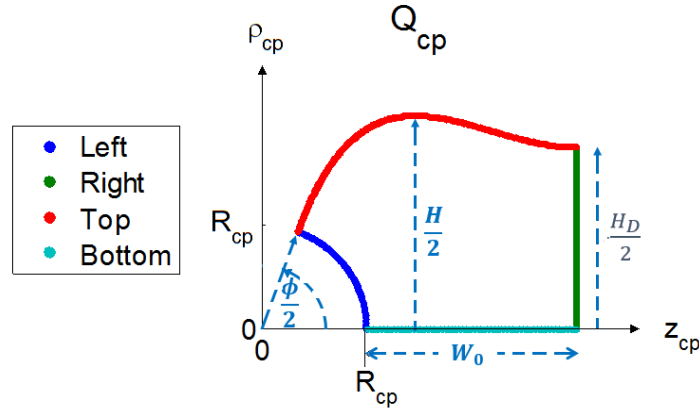

Figure 12: Q_{cp}. Q_{cp} is parameterized by R_{cp}, W_0, ϕ, $\frac{H_D}{2}$ and a (a is directly related to H)

The top side of Q_{cp}, shown in red in Figure 4, is defined by parametric equations, $\left(z_{cp}^{(top)}(s), \rho_{cp}^{(top)}(s)\right)$, which are polynomial functions of s for $0 \leq s \leq 1$. For smoothness, the curve is chosen to have third-order geometric (G³) continuity – i.e. if s represented time, the path's linear and angular acceleration would be continuous. According to [8], the set of polynomials of the lowest order that can be parametric equations of a G³ curve, given any particular set of starting and ending points; starting and ending tangential angles; starting and ending curvatures; and starting and ending angular accelerations, are the seventh-order ones that [8] describes, in which the coefficients are functions of these eight boundary conditions along with six other parameters: $\eta_1, \eta_2, \eta_3, \eta_4, \eta_5$, and η_6. The top side

of Q_{cp} is thus defined by such a pair of polynomials. The starting point $\left(z_{cp}^{(i)}, \rho_{cp}^{(i)}\right)$ and ending point $\left(z_{cp}^{(f)}, \rho_{cp}^{(f)}\right)$ used are the uppermost points of the left and right sides respectively:

$$\left(z_{cp}^{(i)}, \rho_{cp}^{(i)}\right) = \left(R_{cp} \cos\frac{\phi}{2}, R_{cp} \sin\frac{\phi}{2}\right) \tag{46}$$

$$\left(z_{cp}^{(f)}, \rho_{cp}^{(f)}\right) = \left(R_{cp} + W_0, \frac{H_D}{2}\right) \tag{47}$$

Because the boundaries of Q_{cp} are isolines of the conformal $\mathcal{T}_{cp \to \ell}(z_{cp}, \rho_{cp})$, moreover, the right and left sides of Q_{cp} necessarily meet the top and bottom sides of Q_{cp} at right angles. Therefore, the starting and ending tangential angles of the top curve are the ones that form right angles with the adjacent sides. The starting tangential angle is $\psi_i = \frac{\phi}{2}$ and the ending one is $\psi_f = 0°$. In all test cases, the initial and final angular "acceleration" (second-order derivative with respect to s) is arbitrarily set to 0: $\dot{\kappa}_i = 0$, $\dot{\kappa}_f = 0$. Additionally, the initial curvature is set to $-\frac{1}{R_{cp}}$, while the final curvature is set to 0: $\kappa_i = -1/R_{cp}$, $\kappa_f = 0$. "G3-Splines for the Path Planning of Wheeled Mobile Robots" ([8]) furthermore states that, given the boundary conditions, an approximately optimally smooth pair of polynomials is, in many "typical" cases, the one in which η_1 and η_2 are both set to the distance between the starting and ending points, and the other η's are set to 0:

$$\eta_1 = \eta_2 = \left\| \left(z_{cp}^{(f)}, \rho_{cp}^{(f)}\right) - \left(z_{cp}^{(i)}, \rho_{cp}^{(i)}\right) \right\| \tag{48}$$

$$\eta_3 = \eta_4 = \eta_5 = \eta_6 = 0 \tag{49}$$

Based on experimentation, we find that if

$$\eta_1 = \eta_2 = a \left\| \left(z_{cp}^{(f)}, \rho_{cp}^{(f)}\right) - \left(z_{cp}^{(i)}, \rho_{cp}^{(i)}\right) \right\| \tag{50}$$

then variation of the parameter a linearly affects the overall height H of the reimager. ($\frac{H}{2}$ is illustrated in Figure 4.) Thus, $z_{cp}^{(top)}(s)$ and $\rho_{cp}^{(top)}(s)$ are provided by (22) and (23). The a and b coefficients in these formulas are obtained by fitting.

$$z_{cp}^{(top)}(s) = a_0 + a_1 s + a_2 s^2 + a_3 s^3 + a_4 s^4 + a_5 s^5 + a_6 s^6 + a_7 s^7 \tag{51}$$
$$\rho_{cp}^{(top)}(s) = b_0 + b_1 s + b_2 s^2 + b_3 s^3 + b_4 s^4 + b_5 s^5 + b_6 s^6 + b_7 s^7 \tag{52}$$

Table 1 lists the tests performed. The first test is intended to determine the effect on index range of W_0, the depth of the reimager. Test 2 varies H_D, in order to assess the effect of the height of the back detector plane on the index range. Finally, the third test varies the parameter a defined in (21). This test effectively varies the overall height H of the reimager with each trial, and thus assesses the relationship between H and index range.

Table 3: List of Tests

Test #	Q_{cp} Parameter			
	W_0/R_{cp}	ϕ	H_D/R_{cp}	a
1	$\{1.75, 2, \dots, 5.5\}$	180°	2.5	1
2	3.5	180°	$\{.75, 1, \dots, 5.5\}$	1
3	2.5	180°	2.5	$\{0.5, 0.6, \dots, 1.5\}$

Width test

Using the parameters listed in the first row of Table 1, the first test investigates the effect of W_0 on index range. W_0 is varied from $1.75 R_{cp}$ to $5.5 R_{cp}$ in increments of $.25 R_{cp}$. The resulting $\Delta \hat{n}_{cp}^w$ measurements are plotted in Figure 5.
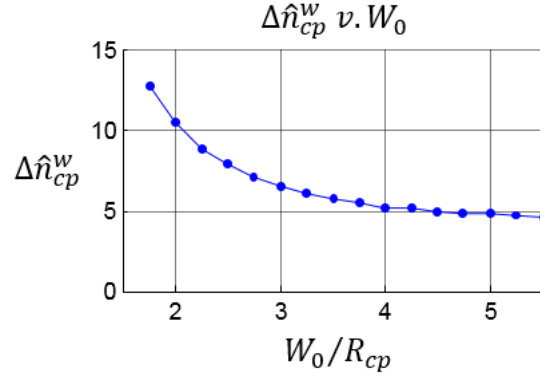
Figure 13: $\Delta \hat{n}_{cp}^w$ $v. W_0$. $\Delta \hat{n}_{cp}^w$ decreases with W_0.

$\Delta \hat{n}_{cp}^w$ decreases with W_0. The reason for this decrease is found by analyzing Figure 6a and b. Figure 6a and b illustrate the paths of ray bundles through the reimager for the two cases in which $W_0 = 1.75R_{cp}$ and $W_0 = 5.5R_{cp}$ respectively. The ray bundles in the longer reimager are bent more gradually, which necessitates a narrower index range, in agreement with the finding that a longer reimager corresponds to a lower $\Delta \hat{n}_{cp}^w$. Based on these results, it is concluded that a longer reimager is more likely to be manufacturable. The larger W_0, the narrower the range of index values is required.
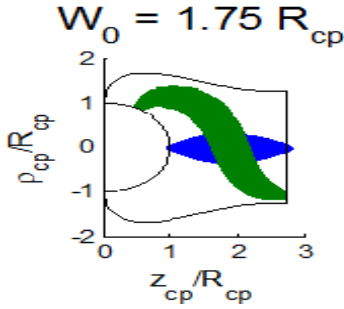

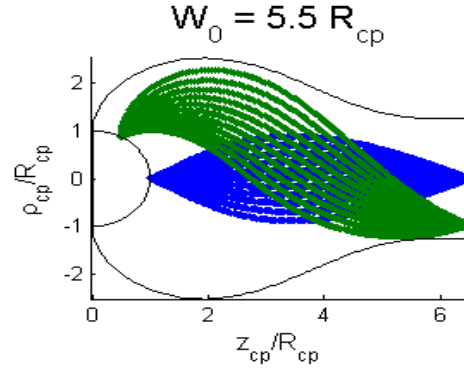Figure 14a: Ray Bundles through Reimager with $W_0 = 1.75R_{cp}$

Figure 6b: Ray Bundles through Reimager with $W_0 = 5.5R_{cp}$

Back height test

In the second test, the effect of the height of the back surface of the reimager, or image height, on the index range is gauged. Q_{cp} is generated with the parameters in the second row of Table 1. H_D, the full height of the back plane of the reimager, is varied from $.75R_{cp}$ to $5.5R_{cp}$ in increments of $.25R_{cp}$. The different Q_{cp}'s corresponding to each test case are shown in Figure 7. The test is created with the hypothesis that the index range is likely to be narrower when H_D is close to values that correspond to an average unit magnification of the image: $H_D \approx \pi R_{cp}$.
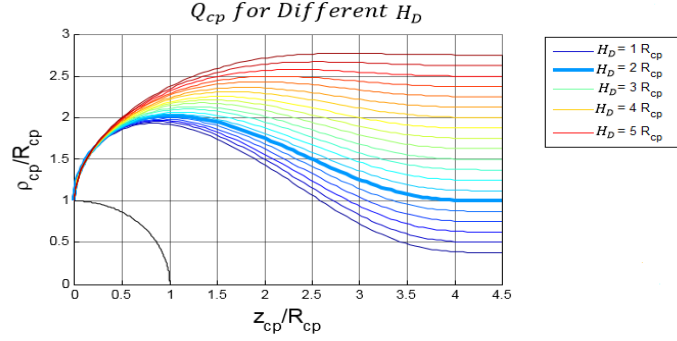
Figure 15: How the Top Side of Q_{cp} varies with H_D. The top side of Q_{cp} terminates at the coordinate $\rho_{cp} = \frac{H_D}{2}$. As H_D is increased, the top side of Q_{cp} becomes smoother. It also becomes taller, which increases the conformal module. As $H_D \to 0$, the back side of Q_{cp} becomes increasingly compressed. The case where $H_D = 2R_{cp}$ is emboldened, since it has the narrowest index range.

The computed $\Delta\hat{n}_{cp}$ for each value of H_D is plotted in Figure 8. For $H_D < 2R_{cp}$, $\Delta\hat{n}_{cp}^w$ decreases with R_{cp}. The narrowest index range occurs for $H_D = 2R_{cp}$. Then, as H_D is increased beyond $2R_{cp}$, the index range widens.

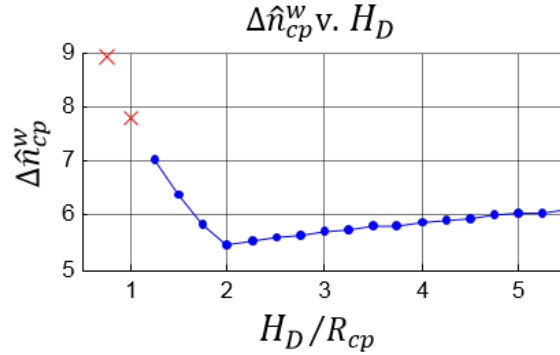
Figure 16: $\Delta\hat{n}_{cp}^w$ v. H_D. $\Delta\hat{n}_{cp}^w$ decreases with H_D for $H_D < 2R_{cp}$ and increases with H_D for $H_D > 2R_{cp}$. (The points with the red x's represent cases in which Q_{cp} does not encompass the area needed for all the rays paths originating within $60°$ of the axis of symmetry.)

This trend is explained by Figure 9a, b, and c, which show traces of ray bundles, from field angles of $0°$ and $60°$, through the reimager for the cases in which $H_D = 0.75R_{cp}$, $H_D = 2R_{cp}$, and $H_D = 5.5R_{cp}$ respectively. (The $60°$ bundle in the $H_D = 0.75R_{cp}$ case is not shown because this Q_{cp} does not encompass enough points to image a $60°$ field of view.) On the one hand, in the case where $H_D = 0.75R_{cp}$, the rays must be abruptly straightened in order to fit inside the compressed back of the reimager. This abrupt change in direction necessitates a wider index range. On the other hand, in the case where $H_D = 5.5R_{cp}$, the $60°$ ray bundle is elongated, compared to the one in the case where $H_D = 2R_{cp}$. A wider index range is also needed for this stretching. In this way, these ray bundle diagrams in Figure 9a-c provide a physical interpretation of the trends in Figure 8.
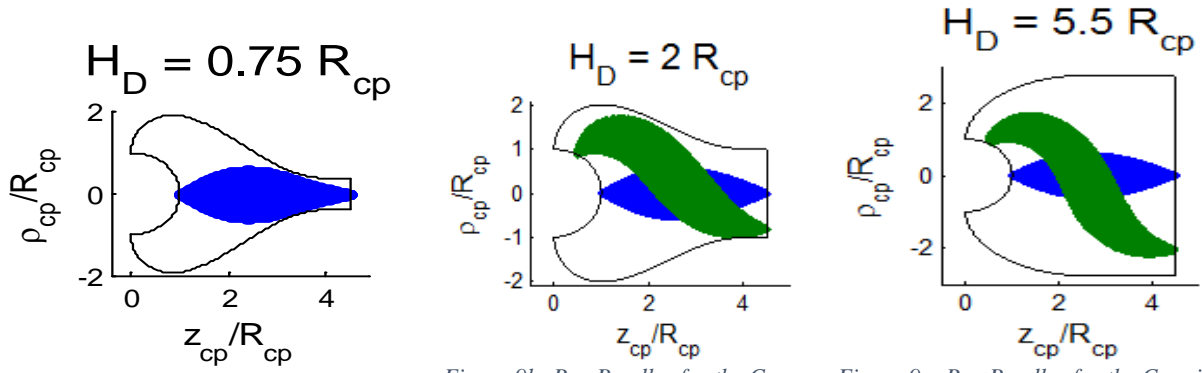
Figure 17a: Ray Bundles for the Case in Which $H_D = 0.75R_{cp}$

Figure 9b: Ray Bundles for the Case in Which $H_D = 2R_{cp}$

Figure 9c: Ray Bundles for the Case in Which $H_D = 5.5R_{cp}$

Traces of ray bundles, from field angles of 0° and 60°. (The 60° bundle in the $H_D = 0.75R_{cp}$ case is not shown because this Q_{cp} does not encompass enough points to image a 60° field of view.) In the case where $H_D = 0.75R_{cp}$, the rays must be abruptly straightened in order to fit inside the compressed back of the reimager. In the case where $H_D = 5.5R_{cp}$, the 60° ray bundle is elongated, compared to the one in the case where $H_D = 2R_{cp}$. Thus the $H_D = 0.75R_{cp}$ and $H_D = 5.5R_{cp}$ cases correspond to a higher $\Delta\hat{n}_{cp}$ and $\Delta\hat{n}_{cp}^w$ than the case in which $H_D = 2R_{cp}$.

This test suggests that there is an optimal H_D for the reimager. In this test, the optimal value is $H_D = 2R_{cp}$. It is anticipated in general, however, that the optimum might depend on the other Q_{cp} parameters, since the value $2R_{cp}$ corresponds to the point at which the set of Q_{cp} repositions the minimum $\left|J_{\ell\to cp}(\mathcal{T}_{cp\to\ell}(z_{cp}, \rho_{cp}))\right|$.

Overall height test

The third test seeks to determine the effect of the overall height of the reimager on index range. It uses the Q_{cp} parameters listed in the third row of Table 1. In order to make the overall height H vary, the parameter a in (21) is changed from .5 to 1.5 in increments of .1. The overall height of Q_{cp} increases linearly with a. This relationship is demonstrated in Figure 10, which illustrates the Q_{cp} corresponding to each tested a, as well as by the measurements of overall height H as a function of a plotted in Figure 11. The test is undertaken with the expectation that the Q_{cp}'s with values of a nearest 1 yield the narrowest index ranges, since their top sides are likely to be the smoothest, according to [8].
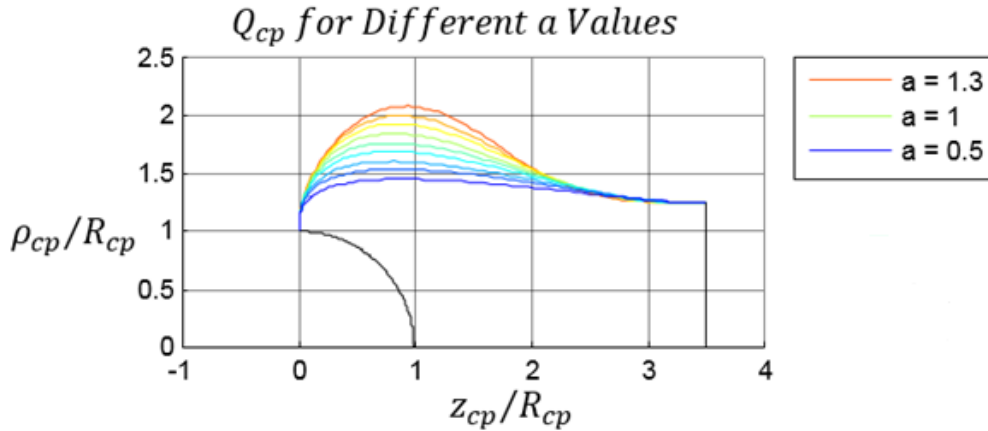

Figure 18: Q_{cp} for Different Values of a. The parameter a is used to vary the overall height of the reimager.
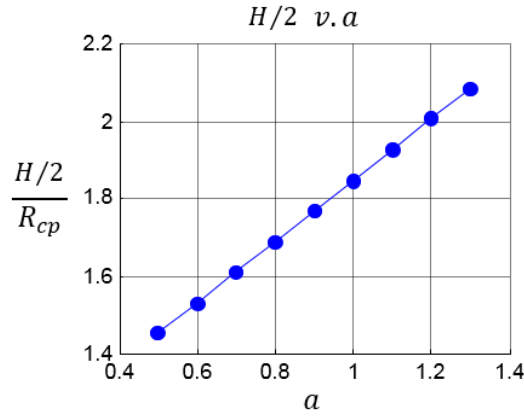
Figure 19: H v. a. For each test case, the overall height H of the reimager is measured. (The parameter H is illustrated in Figure 4.) H varies linearly with a.

The calculated $\Delta\hat{n}_{cp}^{w}$ for each test are plotted in Figure 12 respectively. $\Delta\hat{n}_{cp}^{w}$ is minimal around $a = .7$.
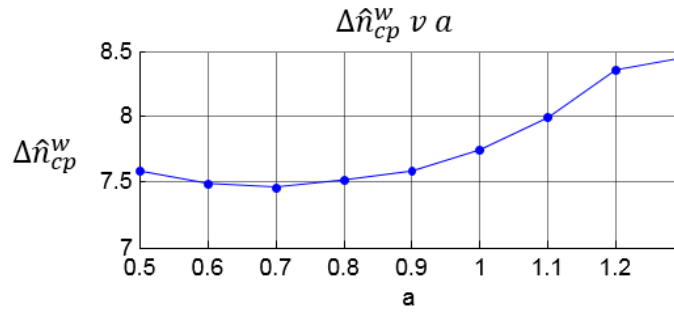

Figure 20: $\Delta\hat{n}_{cp}^{w}$ v. a. The minimum $\Delta\hat{n}_{cp}^{w}$ is at $a \approx .7$.

To help explain the trend in Figure 12, Figure 13a, b, and c show traces of ray bundles, from field angles of $0°$ and $60°$, through the reimager for the cases in which $H = 2.9R_{cp}$, $H = 3.2R_{cp}$, and $H = 4.17R_{cp}$ respectively. The difference between the ray bundle trajectories in the $H = 2.9R_{cp}$ case and the $H = 3.2R_{cp}$ case does not appear significant. On the one hand, in the case where $H = 4.17R_{cp}$, the rays must arch higher. This longer, more arched path explains the necessity for the wider index range associated with the greater heights. In this way, these ray bundle diagrams in Figure 13a-c provide a physical interpretation of the trends in Figure 12.
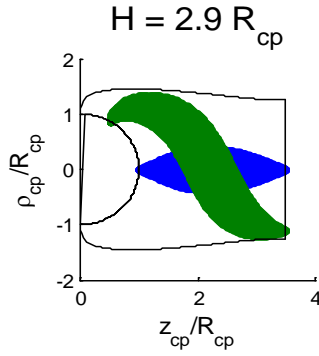
Approved for public release: distribution is unlimited.

| H = 2.9 R$_{cp}$ | H = 3.2 R$_{cp}$ | H = 4.17 R$_{cp}$ |

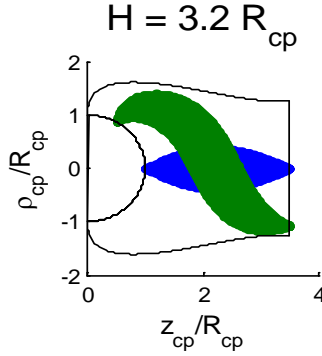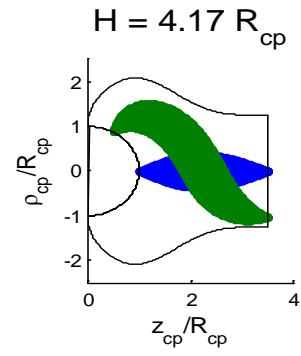*Figure 21a: Ray Bundles for the Case in Which H = 2.9R$_{cp}$* | *Figure 13b: Ray Bundles for the Case in Which H = 3.2R$_{cp}$* | *Figure 13c: Ray Bundles for the Case in Which H = 4.17R$_{cp}$*

Traces of ray bundles, from field angles of 0° and 60°, through the reimager for the cases in which (a) H = 2.9R$_{cp}$, (b) H = 3.2R$_{cp}$, and (c) H = 4.17R$_{cp}$. In the case where H = 4.17R$_{cp}$, the rays must arch higher. This longer, more arched path explains the necessity for the wider index range.

The test results reveal that a and thus H have an optimal value. More vertical room for the reimager beyond the height associated with this optimum is not seen to improve the manufacturability – in fact requiring the light trajectories to take paths that are too high necessitates greater index variation.

After studying the effect of different reimager shape parameters on the range of the constitutive parameters, the material prescriptions for a reimager that can be coupled to the particular monocentric lens specified by [7] are provided, and the optical system is ray-traced to verify that it images as intended. The reimager is designed using a Q_{cp} with $W_0 = 4R_{cp}$, $\phi = 180°$, $H_D = 3.5R_{cp}$, and $H = 4.549R_{cp}$. The calculated constitutive parameters for the reimager needed to reimage a $\pm60°$ field are were computed. Using these parameters bundles of meridional rays are traced through a cross-section of the reimager. Each bundle spans $\pm25°$, approximately the angular extent of the cones of light entering the reimager from the F/1 monocentric lens. (The bundles at larger field angles are expected to have a narrower span, due to surface refraction.) The ray trace is shown in Figure 15, and the spot sizes are shown in Figure 16. The spot sizes of the 30° and 60° field angles at the back surface are less than 2.5 microns – comparable to the size of the fibers bundles. The on-axis rays have a spot size of less than 6 microns. According to transformation optics theory, since the points imaged by Maxwell's fish-eye lens have no finite extent, at least in the geometric limit, then these spot sizes should also be 0. It is therefore not unreasonable to suppose that these small measured spot sizes might be a precision error, either in the discrete model of the constitutive parameters, or in the ray-tracer.
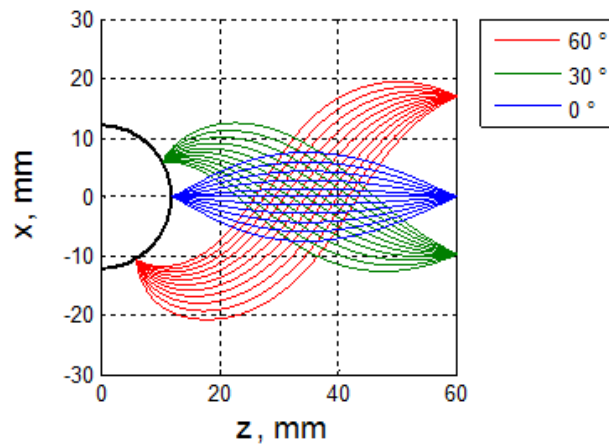

Figure 22: Ray Trace. Bundles of meridional rays, from field angles of 0°, 30°, and 60°, are traced through a cross-section of the reimager. Each bundle spans $\pm25°$.
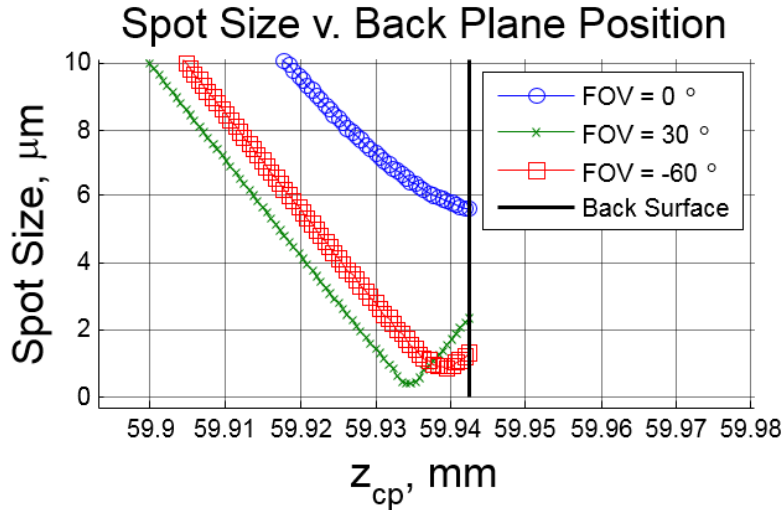
Figure 23: Spot Sizes of Meridional Rays

B.4 - Task 4: Implications for MGRIN.

The MRGIN performers are generally unable to create arbitrary 3D refractive index distributions. It is typical for a specific manufacturing process to yield index distributions with a characteristic symmetry (e.g., layer materials, rotationally symmetric materials, etc.). In this task we have developed a practical design/analysis methodology that can capture these symmetries and enable efficiency optimization.

B.4.a. Refractive index basis functions as a compact representation for complex distributions,

Recent work has demonstrated the principle of transformation optics (TO) [1-4] as a method to design gradient index (GRIN) optical elements. In the TO design method the desired light ray trajectories are first traced through a given material. A transformation is then applied that yields the necessary spatial distribution in permittivity and permeability of that material to yield the desired ray trajectories. Unfortunately, the result of this approach typically yields materials which are highly anisotropic, and/or magnetic, and thus are not readily fabricated. To overcome this barrier a quasi-conformal transform (QCT) optimization approach was developed that removes the need for magnetic materials and minimizes the anisotropy of the TO design [5]. The resulting optical elements only feature spatial variations in the permittivity (refractive index). While the QCT approach is highly effective in some cases it does not always achieve the same performance as the original TO design with magnetic and anisotropic materials. Thus there is a need for further optimization to recover the performance losses that come from TO/QCT GRIN lens designs.

Optimization techniques for GRIN lenses available in commercial ray tracing software (e.g. Zemax, CODE V) typically assume a functional form for the 3D spatial index distribution. Thus the GRIN lens can be parameterized by a relatively few number of coefficients and easily optimized. The GRIN lens designs resulting form TO/QCT generally cannot be represented by the analytic functional forms available in commercial ray tracing software, and thus cannot be easily optimized using these packages. Even if the index profile is manually incorporated into the software using a macro or add-on, the number of free variables (i.e. voxels within the GRIN volume) is so high as to make optimization infeasible. The optimization issues are further exacerbated by the fact that algorithms in ray tracing packages often heavily rely on symmetry and assumptions that may not be valid with these GRIN elements. Thus there is a need for an efficient way to represent and optimize TO/QCT GRIN lens designs.

To accomplish this goal, we propose the use of basis functions to compactly represent the 3D index distribution of the GRIN lens by a relatively few number of coefficients. Using this approach, the 10^6-10^8 voxels for a millimeter

28
Approved for public release: distribution is unlimited.

scale GRIN lens can be accurately represented by less than 1000 coefficients. These coefficients can then be used as the free variables in an optimization algorithm to retrieve the performance of the original TO design. While not as compact as closed form purely analytic GRIN lenses, the basis function approach still yields a feasible optimization problem and gives added freedom to search the design space.

Some relevant questions surrounding this approach include:

- What is the optimal basis for defining GRIN optics?
- How does one choose which and how many coefficients to include in the optimization?
- What is the minimum number of ray and/or field points necessary to properly sample the space within the GRIN lens?

The goal of this initial investigation was to answer some these questions and develop heuristics for the design and optimization of the GRIN lenses using the basis function approach.

B.4.b. A novel ray-tracing engine that can operate on these index representations

A novel design engine was developed in an attempt to answer these questions. The GRIN ray tracing algorithm was based on the work for Sharma et al. [6]. This ray tracer was used as the forward model in the design engine, and the Covariance Matrix Adaptation – Evolutionary Strategy (CMA-ES) algorithm was used as the optimizer [7]. The algorithmic flow through the design engine can be described as follows:

1. Input an initial GRIN lens design that is represented within a given basis
2. A finite number of basis coefficients are kept in order to ensure an accurate representation, and the rest are discarded (i.e. set to zero)
3. The GRIN lens is reconstructed from these finite coefficients, and several bundles of rays are traced through the structure and a figure of merit is calculated (typically RMS spot size)
4. The CMA-ES algorithm adjusts the coefficients and the rays are re-traced through the updated GRIN lens
5. The figure of merit is recalculated and kept if it is smaller than the current minimum
6. Steps 4 and 5 are repeated until the desired FOM is achieved or a fixed number of iterations has been reached

The first study used a standard GRIN lens with a quadratic profile in the transverse dimension and a constant index in the axial dimension as its starting design. This lens was chosen as it is well known in the literature and would serve as a good test case to understand the workings and limitations of the design engine. Additionally, it can be easily represented in Zemax and thus provide validation for our forward model. The input rays were configured such that the lens was focusing collimated rays from five different field points (0°, ±15.35°, ±30.7°) at the back face of the lens. Two different basis functions were used: the discrete cosine transform (DCT) and Daubchies wavelets.

In the first experiment, only the largest valued coefficients from the initial fit were kept for optimization as they yielded the most accurate representation of the initial design. The wavelet basis optimized effectively, however the DCT basis was unable to improve upon the initial design as seen in Fig. 1. The reason for this is that the largest coefficients of the initial fit were only along the transverse dimension, and thus the design engine was unable to alter the axial index profile. This experiment demonstrated an important and not immediately obvious consideration when attempting to optimize GRIN lenses using basis functions: The coefficients which best represent the initial design do are not necessarily the best coefficients for optimization. The DCT optimization was repeated using low frequency coefficients along both dimensions and proceeded to optimize similarly to the wavelets, even though the initial fit was somewhat poor.
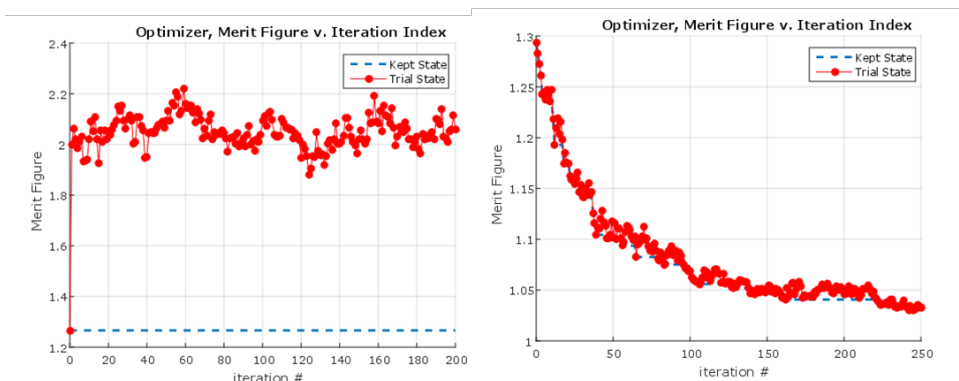
DCT Fit   Daubchies Wavelet Fit

Figure 1

The second experiment attempted to answer the question as to the desired number of coefficients need for optimization. A cursory hypothesis is that more coefficients would give the optimizer more degrees of freedom and lead to better results, but at the cost longer computation times. To test this hypothesis optimization for the quadratic GRIN lens were repeated with an increasing number of coefficients up to 600. It was found that when less than 50 coefficients were used, the initial reconstruction of the GRIN lens was so poor that the rays were not accurately traced through the lens and the optimizer was unable to improve on the design. This provides initial insight on the lower bound on the number coefficients needed for successful optimization. As the number of coefficients was increased the FOM reached a minimum and then steadily began to increase as shown in Fig. 2. This was true for both basis sets with the optimal number of coefficient being near 100. Add more coefficients appears to have created too large of a solution space efficient optimization. The wavelet basis achieved a slightly lower figure of merit, but more rapidly diverged from the optimal result when too many coefficients were used.

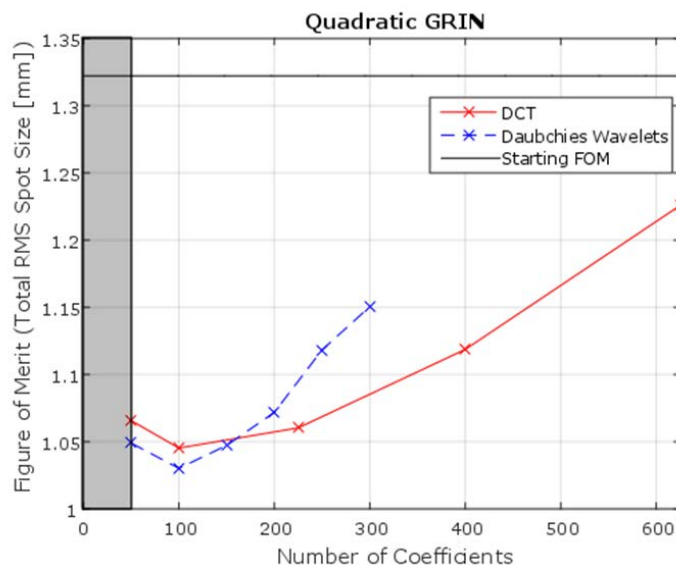
Figure 2

The third experiment in the initial study attempted to determine the minimum number of rays needed to accurately determine the figure of merit. Each ray traced through the system adds to the optimization time, and thus it is imperative to minimize them. However, using too few rays leads to inaccurate sampling the of the lens

30
Approved for public release: distribution is unlimited.

and poor designs. Thus the number of rays needed to effectively optimize was defined as the minimum number of rays such that if the ray density of the bundle of the final design is arbitrarily increased the RMS spot size does not substantially increase. Table 1 shows the results of this experiment for both basis functions. It was found that using 25 rays per bundle in the DCT basis and 30 rays per bundle in the wavelet basis were required to produce less than a 1 μm change in the RMS spot size when 300 rays were traced in the same bundle. This is a logical result as the wavelet basis results in more local high frequency oscillations than the DCT which needs denser sampling. So even though the initial analysis suggests that the wavelet basis yielded better results, it required more rays per bundle (and thus a slower optimization time) to achieve that result.

Average Increase in RMS Spot Size for 300 rays traced per bundle (μm)

Number of Rays per Bundle Used for Optimization	DCT Fit	Wavelet Fit
7	4.4	54.2
15	2.8	7.7
20	1.2	3.3
25	0.7	1.6
30	0.5	0.9

Table 1

Combining the results described thus far one can generally conclude that the basis function approach to GRIN lens design needs a sufficient number of coefficients to effectively represent the initial design, but not so many coefficients as to create an unsearchable space. Furthermore, the distribution of those coefficients should be chosen to ensure that space is not over constrained by the geometry starting design. Finally, the number of rays per bundle should be dense enough as to effectively sample the index distribution within the lens. Applying these heuristics to the quadratic GRIN singlet the basis function approach was able to improve RMS spot size over the full field by an order of magnitude and approach diffraction limited resolution, as shown in Table 2.

Field Point	Zemax Optimized RMS Spot Size (μm)	Optimized DCT Fit RMS Spot Size (μm)	Optimized Wavelet Fit RMS Spot Size (μm)
-30.7°	154.8	18.7	15.2
-15.35°	141.5	11.5	4.4
0°	191.1	7.7	4.2
15.35°	141.5	13.5	5.6
30.7°	154.8	17.5	10.7

Table 2: Both fits optimized with 30 rays per bundle. Spot sizes calculated from 300 traced rays per bundle. Diffraction limited spot size is 1.68 μm.

B.4.c. Some results that show how much better/faster this approach can be.

The results thus far demonstrate the potential of basis functions as tool for efficient optimization of a GRIN lens, but only on a test case. To demonstrate the design engine in the intended application a TO/QCT design for relay imager was used in the second study. The relay imager was based off of the Luneburg lens, and TO/QCT was used

Approved for public release: distribution is unlimited.

to make the input side concave and the output side flat. The relay imager is intended to be used a monocentric camera. The initial TO/QCT design for the imager can be seen in Fig. 3.
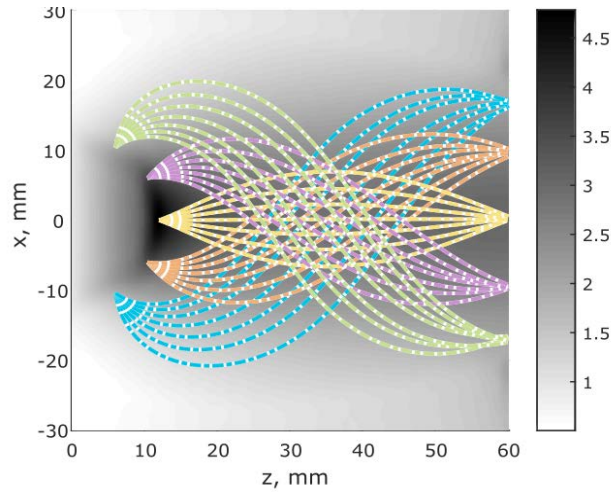

Figure 3

The relay imager was optimized using both the DCT and wavelet bases using an increasing number of coefficients. The largest coefficients were used for this simulation given that the initial design featured sufficient variation in both the transverse and axial directions. The behavior of this lens with respect to the number of optimization coefficients was far less predictable than the quadratic GRIN, as shown in Fig. 4. Again the wavelet basis reached the best result at 100 coefficients, but there is evidence to indicate that the solutions do not get monotonically worse with increased number of coefficients.
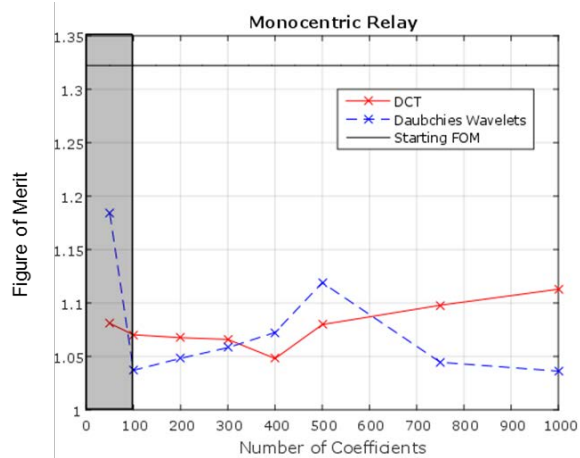

Figure 4

The best overall design is shown in Fig. 5, and featured spot sizes of 7.0, 8.9, 9.9, 7.8 and 3.4 microns across the field of view. The final figure of merit was an order of magnitude improvement over the initial design.
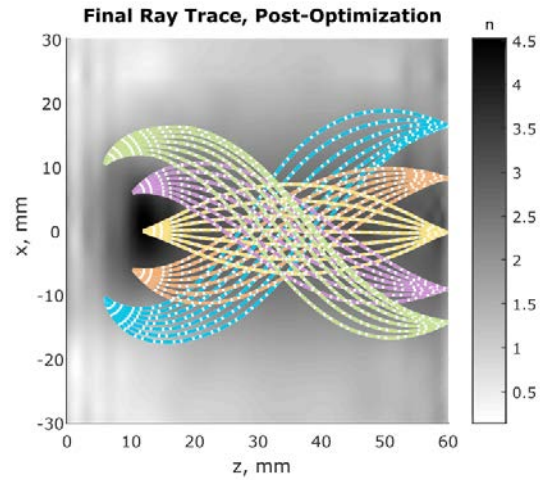
Figure 5

Due to the obvious dependence on initial conditions and lens geometry, it is difficult to make conclusive and far reaching determinations from this initial study. However, it was clearly demonstrated that the basis function approach to optimization has the ability significantly improve the performance of the TO/QCT GRIN lens designs.

Bibliography

Section A

[1] A. Rogalski, "Progress in focal plane array technologies," *Progress in Quantum Electronics*, Vol. 36, pp. 342-473, 2012.

[2] J. L. Tissot, "IR detection with uncooled focal plane arrays, state-of-the art and trends," *Opto-Electronics Review*, Vol. 12, pp. 105-109, 2004.

[3] D. J. Brady, "Optical Imaging and Spectroscopy," Chapter 10 – Computational Imaging, *Wiley*, 2009.

[4] M. Levoy, "Light Fields and Computational Imaging," *IEEE Computer Magazine*, Vol. 39, pp. 46-56, 2006.

[5] E. R. Dowski and W. T. Cathey, "Extended depth of field through wave-front coding," *Applied Optics*, Vol. 34, pp. 1859-1866, 1995.

[6] M. A. Neifeld and J. Ke, "Optical architectures for compressive imaging," *Applied Optics*, Vol. 46, pp. 5293-5303, 2007.

[7] T. Adelson and J.Y.A. Wang, ''Single Lens Stereo with a Plenoptic Camera,'' IEEE Trans. Pattern Analysis and Machine Intelligence, Vol. 14, pp. 99-106, 1992.

[8] E. Clarkson and H. Barrett, "Bounds on null functions in digital imaging systems," *Journal of the Optical Society of America A*, Vol. 15, pp. 1355-1360, 1998.

[9] W. T. Cathey and E. R. Dowski, "New paradigm for imaging systems," *Applied Optics*, Vol. 41, pp. 6080-6092, 2002.

[10] W. Chi and N. George, "Computational imaging with the logarithmic asphere: theory," *Journal of the Optical Society of America A*, Vol. 20, pp. 2260-2273, 2003.

[11] E. J. Tremblay et al. "Relaxing the alignment and fabrication tolerances of thin annular folded imaging systems using wavefront coding," *Applied Optics*, Vol. 46, pp. 6751-6758, 2007.

[12] M. F. Duarte, M. A. Davenport, D. Takhar, J. N. Laska, S. Ting, K. F. Kelly, and R. G. Baraniuk, "Single-pixel imaging via compressive sampling," *IEEE Signal Processing Magazine*, Vol. 25, pp. 83–91, 2008.

[13] M. A. Neifeld and P. Shankar, "Feature-specific imaging," *Applied Optics*, Vol. 42, pp. 3379-3389, 2003.

[14] P. K. Baheti and M. A. Neifeld, "Recognition using information optimal adaptive feature-specific imaging," *Journal of the Optical Society of America A*, Vol. 26, pp. 1055-1070, 2009.

[15] H. Pal and M. A. Neifeld, "Multispectral principal component imaging," *Optics Express*, Vol. 11, pp. 2118-2125, 2003.

Section B.3

[1] J. Li and J. Pendry, "Hiding under the Carpet: A New Strategy for Cloaking," *Phys. Rev. Lett.,* p. 203901, 2008.

[2] N. I. Landy, N. Kundtz and D. R. Smith, "Designing Three-Dimensional Transformation Optical Media Using Quasiconformal Coordinate Transformations," *Physical Review Letters,* p. 193902, 2010.

[3] Llamas, inc., "AWARE2 Multiscale Gigapixel Camera," 4 February 2014. [Online]. Available: http://www.disp.duke.edu/projects/AWARE. [Accessed 4 December 2015].

[4] "New Optics Can Capture Wide Fields in Exquisite Detail," 9 October 2013. [Online]. Available: http://spectrum.ieee.org/tech-talk/semiconductors/optoelectronics/wide-fields-in-exquisite-detail.

[5] J. F. Thompson, B. K. Soni and N. P. Weatherill, Handbook of Grid Generation, Boca Raton: CRC Press LLC, 1999.

[6] P. Knupp and S. Steinberg, Fundamentals of Grid Generation, Boca Raton: CRC Press, 1994.

[7] I. Stamenov, I. P. Agurok and J. E. Ford, "Optimization of two-glass monocentric lenses for compact panoramic imagers: general aberration analysis and specific designs," *Applied Optics,* pp. 7648-7661, 2012.

[8] A. Piazzi, M. Romano and C. Guarino Lo Bianco, "G3-Splines for the Path Planning of Wheeled Mobile Robots," in *European Control Conference*, Cambridge, 2003.

[9] A. Arianpour, I. Agurok, N. Motamedi and J. E. Ford, "Enhanced Field of View Fiber Coupled Image

Sensing," *Classic Optics,* 2014.

[10] I. Stamenov, A. Arianpour, S. J. Olivas, I. P. Agurok, A. R. Johnson, R. A. Stack, R. L. Morrison and J. E. Ford., "Panoramic monocentric imaging using fiber-coupled focal planes," *Optical Society of America,* 2014.

[11] N. Landy, Y. Urzhumov and D. R. Smith, "Quasi-Conformal Approaches for Two and Three-Dimensional Transformation Optical Media," in *Transformation Electromagnetics and Metamaterials*, London, Springer-Verlag, 2014.

[12] J. B. Pendry, D. Schurig and D. R. Smith, "Controlling Electromagnetic Fields," *Science,* pp. 1780-1782, 2006.

[13] J. Li and J. B. Pendry, "Hiding under the Carpet: A New Strategy for Cloaking," *Phys. Rev. Lett.,* p. 203901, 2008.

[14] D. R. Smith, Y. Urzhumov, N. B. Kundtz and N. I. Landy, "Enhancing imaging systems using transformation optics," *Optics Express,* pp. 21238-21251, 2010.

[15] H. F. Ma and T. J. Cui, "Three-dimensional broadband and broad-angle transformation-optics lens," *Nature Communications,* 2010.

[16] J. E. Ford, I. Agurok and I. Stamenov.United States of America Patent WO2014074202A2, 2014.

[17] S. J. Olivas, A. Arianpour, I. Stamenov, R. Morrison, R. A. Stack, A. R. Johnson, I. P. Agurok and J. E. Ford, "Image processing for cameras with fiber bundle image relay," *Applied Optics,* pp. 1124-1137, 2015.

[18] SCHOTT North America, Inc., "SCHOTT Fiber Optic Faceplates," July 2013. [Online]. Available: http://www.us.schott.com/lightingimaging/english/download/schott-faceplate_us_july_2013.pdf.

[19] T. Sutton, "An improved panoramic lens for taking photographic pictures". United Kingdom Patent 2193, 28 September 1859.

[20] C. Lord, "Comments on Gary Seronik's TMB Monocentric Eyepiece test report Sky & Telescope Aug. 2004 pp98-102," 20 December 2005. [Online]. [Accessed 22 October 2015].

[21] S.-B. Rim, P. B. Catrysse, R. Dinyari, K. Huang and P. Peumans, "The optical advantages of curved focal plane arrays," *Optics Express,* pp. 4965-4971, 2008.

[22] H. H. Windsor, "Spherical Camera," *Popular Mechanics Magazine,* pp. 94-95, March 1953.

[23] S. Karbasi, N. Motamedi, A. Arianpour, W. M. Mellete and J. E. Ford, "Analysis and compensation of moire effects in fiber-coupled image sensors," *SPIE,* vol. 9579, pp. 957910 1-8, 2015.

[24] D. Dumas, M. Fendler, N. Baier, J. Primot and E. le Coarer, "Curved focal plane detector array for wide field cameras," *Applied Optics,* vol. 51, no. 22, pp. 5419-5424, 2012.

[25] H.-C. Jin, J. R. Abelson, M. K. Erhardt and R. G. Nuzzo, "Soft lithographic fabrication of an image sensor on a curved substrate," *Journal of Vacuum Science and Technology B,* vol. 22, pp. 2548-2551, 2004.

[26] D. L. Marks and D. J. Brady, "Gigagon: a Monocentric Lens Design Imaging 40 Gigapixels," *OSA technical Digest (CD),* 2010.

[27] D. L. Marks, E. J. Tremblay, J. E. Ford and D. J. Brady, "Microcamera aperture scale in monocentric gigapixel cameras," *Applied Optics,* vol. 50, no. 30, pp. 5824-5833, 2011.

[28] A. Nicolet and F. zolla, "Cloaking with Curved Spaces," *Science,* vol. 323, pp. 46-47, 2009.

[29] M. Born and E. Wolf, Principles of Optics, 6th Ed., Cambridge: Cambridge University Press, 1998.

[30] S. Zhang, "Invisibility Cloak at Optical Frequencies," in *Tranformation Electromagnetics and Metamaterials*, Springer-Verlag, London, 2014, p. 290.

[31] J. K. Wetherill, R. N. Zahreddine, R. S. Lepkowicz and M. A. Neifeld, "Transformation optics relay lens design for imaging from a curved to a flat surface," in *Advanced Optics for Defense Applications*, Baltimore, 2016.

[32] C. Kottke, A. Farjadpour and S. G. Johnson, "Perturbation theory for anisotropic dielectric interfaces, and application to subpixel smoothing of discretized numerical methods," *Phys. Rev. E, 77,* 2008.

[33] J. Rolland and K. Thompson, "Freeform optics: Evolution? no, revolution!," 19 July 2012. [Online]. Available: http://spie.org/newsroom/4309-freeform-optics-evolution-no-revolution. [Accessed 18 May 2016].

Section B.4

1. J. B. Pendry, D. Schurig, and D. R. Smith, "Controlling electromagnetic fields.," Science **312**, 1780–1782 (2006).
2. D. R. Smith, Y. Urzhumov, N. B. Kundtz, and N. I. Landy, "Enhancing imaging systems using transformation optics," Opt. Express **18**, 21238–21251 (2010).
3. D. A. Roberts, N. Kundtz, and D. R. Smith, "Optical lens compression via transformation optics," Opt. Express **17**, 16535–16542 (2009).
4. D. Liu, L. H. Gabrielli, M. Lipson, and S. G. Johnson, "Transformation inverse design," Opt. Express **21**, 14223–14243 (2013).
5. J. Li and J. B. Pendry. Hiding under the carpet: a new strategy for cloaking. Physical Review Letters, 101:203901, (2008).
6. A. Sharma, D. Vizia Kumar, and A. K. Ghatak, "Tracing rays through graded-index media: a new method.," Appl. Opt. **21**, 984–987 (1982).
7. Hansen, N., "The CMA evolution strategy: a comparing review", *Towards a new evolutionary computation. Advances on estimation of distribution algorithms*, Springer, 1769–1776 (2006).